IACMI/R006-2020/6.14

Smart Composite Pressure Vessels (SCPV) with Integrated Health Monitoring

Participating organizations:

Steelhead Composites,

University of Tennessee, Knoxville,

Teijin America,

Oak Ridge National Laboratories,

LUNA

Date: April 2020

Final Technical Report

PA16-0349-6.14-01

Approved for Public Release.
Distribution is Unlimited.

THE COMPOSITES INSTITUTE

U.S. DEPARTMENT OF ENERGY

DOCUMENT AVAILABILITY

Reports produced after January 1, 1996, are generally available free via US Department of Energy (DOE) SciTech Connect.

Website http://www.osti.gov/scitech/

Reports produced before January 1, 1996, may be purchased by members of the public from the following source:

National Technical Information Service
5285 Port Royal Road

Springfield, VA 22161

Telephone 703-605-6000 (1-800-553-6847)

TDD 703-487-4639

Fax 703-605-6900

E-mail info@ntis.gov

Website http://www.ntis.gov/help/ordermethods.aspx

Reports are available to DOE employees, DOE contractors, Energy Technology Data Exchange

The information, data, or work presented herein was funded in part by the Office of Energy Efficiency and Renewable Energy (EERE), U.S. Department of Energy, under Award DE-EE0006926

Smart Composite Pressure Vessels (SCPV) with Integrated Health Monitoring

Principal Investigator: Kaushik Mallick

Organization: Steelhead Composites

Address: 500 Corporate Circle, Ste O, Golden, CO 80401

Phone: (720) 524-3360

Email: kmallick@steelheadcomposites.com

Co-authors: Dayakar Penumadu, Gregory Lambert, Robert Norris, B.K. Khoo, Aida Rahim

Date Published: (April 2020)

Prepared by:

Institute for Advanced Composites Manufacturing Innovation

Knoxville, TN 37932

Managed by Collaborative Composite Solutions, Inc.

For the

U.S. DEPARTMENT OF ENERGY

Under contract DE- EE0006926

Project Period:

05/2018 – 09/2019

Approved For Public Release

TABLE OF CONTENTS

1. Lists

1.1 List of Figures

1.2 List of Tables

1.3 List of Acronyms

COPV	Composite Overwrapped Pressure Vessels
STEB	Standard Test and Evaluation Bottle
FEA	Finite Element Analysis
HD-DFOS	high-definition distributed fiber optic sensors
BVID	Barely visible impact damage
DOE	Department of Energy
SHC	Steelhead Composites
UTK	University of Tennessee, Knoxville

2. EXECUTIVE SUMMARY

The U.S. Department of Energy (DOE) is promoting and developing more energy efficient and environmentally friendly technologies that will enable America to use less petroleum. Hydrogen fuel cells – which directly convert the chemical energy in hydrogen to electricity with only water and heat as byproducts – are a very attractive solution that can enable this to happen. To date, DOE's efforts have culminated in commercial demonstration of on-board vehicular hydrogen storage systems that can allow for a driving range of greater than 300 miles. This requires storing 5 Kgs of hydrogen onboard a light vehicle. In order to store this quantity of hydrogen, the hydrogen gas needs to be stored in a composite overwrapped pressure vessel (COPV) at a very high internal pressure.

The objective of the program was to demonstrate continuous and predictable health-monitoring of composite pressure vessels. A higher confidence in the operational safety of the vessels will lead to reduced burst factor of safety imposed by regulatory standards and hence will help reduce the structural wall thickness that drives the cost of the vessel.

Highly optimized Type III (metal lined) and Type IV (polymer lined) COPVs that are manufactured using filament winding process have been designed and qualified for the above mentioned application. However, the main structural component of the COPVs is carbon fiber and the high cost of carbon fiber composite in a pressure vessel is a primary challenge in reducing the cost of gaseous hydrogen storage. Continuous and remote monitoring of structural health of the COPVs as well as optimization of the strength translation of carbon fibers have the potential to allow for reduced factor of safety, thereby reduced amount of carbon and associated cost of the vessel.

In the current program, the project team including Steelhead Composites (SHC), University of Tennessee, Knoxville (UTK), Teijin Carbon America, Oak Ridge National Laboratory (ORNL) and LUNA designed, fabricated, and tested smart composite pressure vessels with integrated sensors. Iterative loops of design and testing using coupons, subscale STEB vessels and full size vessels proved that a new generation of high performance carbon fiber can be used for efficient design of Type 3 vessels for H2 storage. Novel analysis techniques were developed to predict the initiation and propagation of interlaminar damage inside the composite shell due to impact damage, a real threat in practical operation. Such an analysis scheme is typically not used in tank design but is an essential tool for health monitoring of composite vessels. Remote sensing of the key signatures of the tank's operating parameters such as pressure, acceleration and humidity was demonstrated using a unique device that can wirelessly transmit and stream the data to a remote server. Fiber optic sensors were successfully integrated during fabrication of the tanks. These sensors provide a wealth of information regarding the structural health of the vessel when it is subsequently pressurized or subjected to impact damage. Excellent correlation was demonstrated between the fiber optic sensor and mechanical strain gage data, and between the measurements and analytical predictions.

3. INTRODUCTION

Steelhead Composites has been in the forefront of commercializing H2 storage vessels not only for automotive (automobiles and bus) applications, but for marine, transportation, autonomous drones and aerospace applications as well. The company sees onboard health monitoring for COPVs to be a crucial technology to assure safety, reduce cost and prolong 'safe life' in these highly complex pressure-bearing structures. The company has also explored multiple state-of-the-art sensing technologies only to realize that they are difficult to integrate with traditional vessel manufacturing and/or require complex and expensive black-box devices that need to be hooked up to the sensors for continuous monitoring. These factors have inspired Steelhead Composites to search for a cost-effective solution that can be integrated with COPV during its manufacturing process and one that stays with the vessel cradle-to-death.

The manufacturing process for compressed gas storage vessels typically uses the filament winding technique which employs numerically controlled delivery heads to wrap successive layers of reinforcing fibers according to a pre-designed lamination scheme on a liner. Steelhead Composites currently use fibers impregnated in epoxy matrix or towpregs during the winding process, with plans to consider thermoplastic based resin system for improved toughness, damage resistance and recyclability of the composite pressure vessels. Carbon is the material of choice for the reinforcing fiber due to its high strength to weight ratio, excellent stress-rupture, and fatigue characteristics. However, carbon fiber is expensive and constitutes 60-70% of the cost of the finished composite pressure vessel. Serial production of composite pressure vessels necessary for wide adoption of fuel cell cars will necessitate optimization of the cost of the composite pressure vessels, which in turn will require judicious use of the composite overwrap. Most composite pressure vessels are designed to regulatory standards that mandate safety factors against burst, stress rupture, pressure cycles, impact damage and flaw tolerance. These safety factors all have lineage to the aerospace heritage of composite pressure vessels. Real time monitoring of the structural health is sought to minimize the padded safety factors without sacrificing the safety of the vessels.

4. BACKGROUND

4.1 Hydrogen as Energy Carrier

There is significant interest in exploring how the United States can reduce dependence on imported oil and move towards energy solutions that are more sustainable. The U.S. Department of Energy (DOE) is promoting and developing more energy efficient and environmentally friendly technologies that will enable America to use less petroleum [1]. Hydrogen fuel cells – which directly convert the chemical energy in hydrogen to electricity with only water and heat as byproducts – are a very attractive solution that can contribute to achieving these goals. The mission of DOE's vehicles programs such as H2@Scale [1], the Hydrogen, Fuel Cells and Infrastructure Technologies (HFCIT), and FreedomCAR is to research, develop, and validate hydrogen production, storage, and fuel cell technologies and to overcome the non-technical barriers to the commercialization of these technologies [3]. The long-term aim is to develop "leapfrog" technologies that will provide Americans with greater freedom of mobility and energy security, while lowering costs and reducing impacts on the environment.

Hydrogen is an ideal energy carrier with high energy content per unit mass that can help increase our energy diversity and security by reducing our dependence on hydrocarbon-based fuels. Hydrogen can be produced from domestic resources, including renewable energy sources that are clean, diverse, and abundant. Fuel cells provide a technology to use the energy stored in hydrogen in a highly efficient way and in numerous applications, with only water and heat as byproducts. As part of the DOE's Hydrogen program, several industries are looking into the best ways to use fuel cells to power automobiles and heavy vehicles [4]. DOE's initiative and push has already put fuel cell buses on the road and may soon put new fuel-cell powered vehicles on the nation's rails and waterways (Figure 1).

(a)

(b)

(c)

FIGURE 1: COPVS FOR H2 STORAGE ARE REQUIRED FOR DIVERSE MARKETS RANGING FROM (A) AUTOMOTIVE SUCH AS GENERAL MOTOR'S CHEVROLET COLORADO ZH2 [1] (B) TRUCKS SUCH AS NIKOLA ONE [2] TO (C) MARINE APPLICATIONS SUCH AS DAEDALUS YACHTS [3]

4.2 Challenges in gaseous H2 storage

Unfortunately, due to the very low density of hydrogen, a large volume is required to store large quantities of energy. Recently, DOE's efforts have focused on the R&D of on-board vehicular hydrogen storage systems that will allow for a driving range of greater than 300 miles while meeting packaging, cost, safety, and performance requirements to be competitive with current vehicles. This requires storing 5 Kgs of hydrogen onboard a light vehicle. In order to store this quantity of hydrogen in a light vehicle, the hydrogen gas needs to be stored in a tank with 700 bar (10,000 psi) of internal pressure. Highly optimized Type III (metal lined) and Type IV (polymer lined) composite overwrapped pressure vessels that are manufactured using the filament winding process have been designed and qualified for this application.

A critical challenge lies in the cost of the carbon fibers used in the manufacturing of these tanks as well as in the high cost of the manufacture of composite tanks. High-strength carbon fiber (like Toray's T700S) is typically used in manufacturing the structural shell of these lightweight composite pressure vessels. Unfortunately, current high-

[1] https://media.gm.com/media/us/en/gm/news.detail.html/content/Pages/news/us/en/2016/oct/1003-zh2.html

[2] https://nikolamotor.com/one

[3] http://www.daedalusyachts.com/

strength carbon fiber products are far too expensive to meet DOE goals for storage system costs. The cost of carbon fiber alone constitutes over 50% of the total cost of the pressure vessel. For example, a recent analysis of the costs for 700 bar hydrogen storage systems for light-duty vehicles indicated that at an annual manufacturing rate of 100,000 systems per year, the CF accounts for approximately 52% of the total system cost of $16/kWh of hydrogen (Figure 2) [4]. Most composite pressure vessels are designed to regulatory standards that mandate safety factors against burst, stress rupture, pressure cycles, impact damage and flaw tolerance. These safety factors have lineage to the aerospace heritage of composite pressure vessels with low burst factor (1.5 – 2x) and low fatigue cycles (100-1000s). The safety factors have not been critically fine-tuned for higher burst factor (2.25 – 3x) and high fatigue cycle application (20,000 -100,000s) of automotive or transportation industry. The safety (burst) factors referred to in the design standards for the latter applications also assume manufacturing variability, workmanship and damage tolerance not inherently included in the design. Real time monitoring of the structural health is sought to minimize the padded safety factors without sacrificing the safety of the vessels.

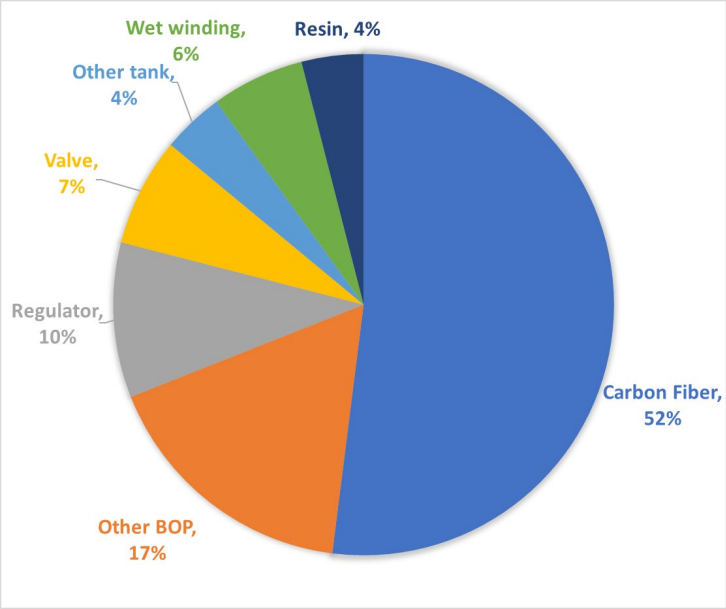

FIGURE 2: COST BREAKDOWN IN A H2 STORAGE FOR HIGH VOLUME PRODUCTION

4.3 Need for continuous health monitoring

Steelhead Composites sees onboard health monitoring for COPVs to be a crucial technology to assure safety, reduce cost and to prolong the life in these highly complex, pressure bearing structures. Carbon is the material of choice for the reinforcing fiber due to its high strength to weight ratio, as well as excellent stress-rupture and fatigue characteristics. However, carbon fiber composites also pose a serious challenge in that damage due to impact and interlaminar damage due to fatigue are very hard to detect from external appearance. Therefore, the purpose of health monitoring is to detect incipient faults in the composite shell due to impact and/or predict the number of cycles to its end of life in leak-before-burst failure mode

Continuous structural health monitoring has important practical implications such as reducing maintenance costs and increasing operational safety of COPVs. One of the critical needs for continuous health monitoring is keeping an ongoing record of the COPV's fill-and-drain cycles and to provide immediate feedback on the vessel's structure in response to any unplanned damage caused by either low or high energy impact. The ultimate goal of health

monitoring is to allow for higher confidence in the design factor of safety of the vessels thereby reducing the amount and cost associated with the critical pressure-bearing composite structure.

5. RESULTS AND DISCUSSION

5.1 Develop and Validate advanced analytical tools to predict damage in composite pressure vessels

One of the key goals of the program is to enable structural health monitoring of composite pressure vessels such that unexpected damage to the structure can be detected and evaluated. Without proper evaluation of the state of the structural integrity of the COPV, there is risk of needlessly discarding a vessel with acceptable level of damage.

Typically, damage imparted to a COPV from impact is hard to detect by visual observation. Impact damage can cause interlaminar failure as well as fiber fracture in the inner plies of the COPV that will be hard to detect without embedded sensors. Analytical tools are needed to correlate the degree of such complex failure modes in composites to the information collected from the sensors to make a decision on the structural integrity of the COPV. In order to distinguish critically damaged vessels from those with less severe or benign damage, detailed knowledge of how the damaged composite behave is needed. This includes understanding how the damage propagates during the impact event as well as how the damage may propagate under cyclic pressure load that the COPV may be subjected to after the impact.

Much research has been done in the field of FEA simulation of composite damage. However, most are limited to flat panels and simplified geometry. There has been limited research on damage in filament wound pipes, but the understanding of the subject is quite limited. Therefore, the current task focused on developing a 3D model for filament wound composite vessel in ABAQUS using continuum elements for the main composite plies as well as cohesive elements to model interlaminar failure between the plies. The objective was to demonstrate and validate a robust analytical tool that can accurately predict complex damage patterns in a COPV subjected to low to medium velocity impact. Cohesive elements are purpose designed elements to model the behavior of adhesive joints and interfaces in composite materials. For the current effort, three dimensional cohesive elements (COH3D8) are used in addition to continuum shell elements (SC8R) used for individual composite plies in a COPV (Figure 3).

Figure 4(a) shows the experimental set-up at of the drop impact test on a composite pressure vessel at University of Tennessee. Figure 4(b) shows the 3D finite element model created by Steelhead Composites to simulate the drop impact test. The model uses a Type 3 vessel construction with 6061-T6 Aluminum liner with composite overwrap designed for 350 bar H2 storage. A full elastic-plastic material behavior is assumed for the Aluminum. The composite overwrap consists of multiple plies of unidirectional composite arranged in specific order and with varying angles of orientation relative to the vessel axis that represent the filament wound layers of construction. In addition to the individual plies, the composite shell also incorporates interlaminar plies modeled using cohesive layers inserted between the individual filament wound layers.

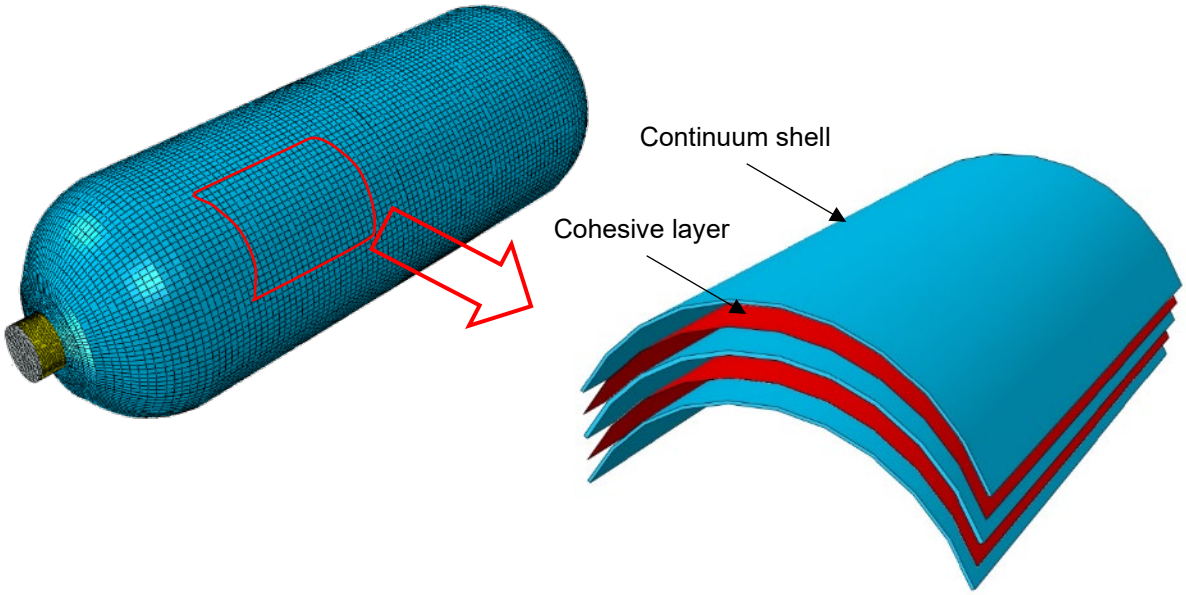

FIGURE 3: 3D FINITE ELEMENT MODEL OF A COPV INCORPORATING COHESIVE LAYERS TO PREDICT INTERLAMINAR DAMAGE

(a) (b)

FIGURE 4: 3D FINITE ELEMENT MODEL OF AN 80 L DESIGNED FOR 5000 PSI H2 STORAGE

The impact is simulated using a vertical travel of a 50.8 mm (2 in.) diameter x 12.7 mm (0.5 in.) thick disc with velocity of 37.8 m/sec (1488 in/sec) assigned to produce 50 J (442.44 in-lbs) of energy during the impact. The analysis is performed using explicit finite element analysis in ABAQUS finite element software. Figure 5 shows the results in the composite shell after the impact. Assuming the unidirectional composite material in the vessel overwrap consists of Teijin ITS50-24K carbon fiber[4] with a 60% fiber volume fraction, the tensile strength is estimated to be 3060 MPa (443,700 psi). Per the FEA results, the maximum principal stresses (808 MPa / 117,200 psi) in the composite plies (Figure 5(a)) are well below the tensile strength of the carbon fiber composite. However, the degree of damage, D (loss of stiffness) in the interlaminar plies is indicated in the contour plot of SDEG, with values greater than 0. Some areas close to the area of impact as well as in zones away from the impact indicate significant loss of stiffness with values of D ≈ 1. The simulation results confirm how challenging it is to detect impact damage on the composite shell without the confirmation of fiber breakage. The loss of stiffness caused by the interlaminar damage in the structural shell causes stress risers in the shell as well as the liner underneath. Through the pressurization cycles, such weakness can manifest itself in fatigue failure of the liner and eventually to leakage of fluids. Simulation results and their validation through health monitoring are essential to predict and detect the interlaminar damage incurred in the COPV from low velocity impacts and to warn the monitoring system and the user of the extent of the damage from impact.

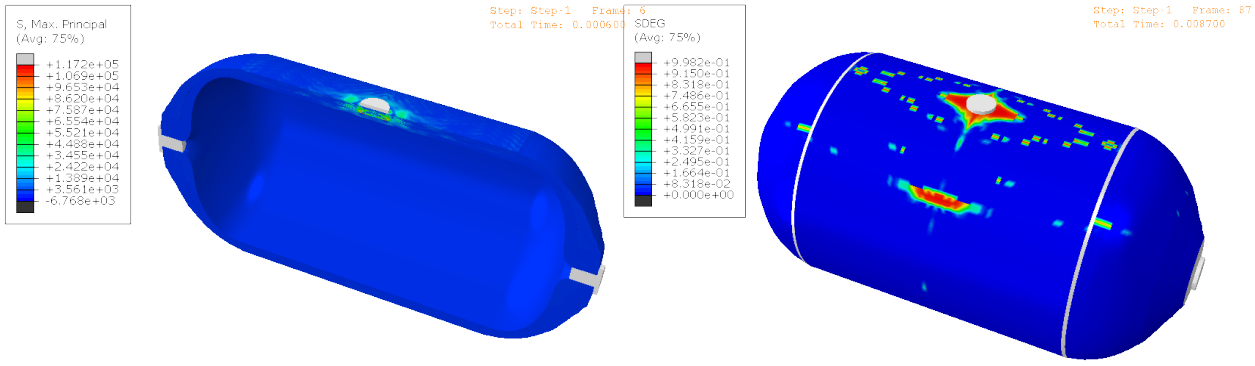

(a) (b)

FIGURE 5: (A)INTRALAMINAR STRESSES AND (B) INTERLAMINAR DAMAGE IN THE COMPOSITE SHELL OF COPV DURING IMPACT

[4] https://www.teijincarbon.com/fileadmin/PDF/Datenbl%C3%A4tter_en/Filament-Product_programm__EU__v27_2018-06-27_EN.pdf

5.2 Fiber Strength Translation and Optical Sensor Integration Using a Standard Test and Evaluation Bottle (STEB)

Strength translation from a carbon fiber tow to a corresponding fiber-reinforced polymer composite typically depends on the polymer, fiber volume, adhesion between the fiber and the resin, and defects found on fibers. Furthermore, this strength translation is further affected by the processing conditions when the fibers are applied on a COPV during the filament winding process. Since one of the program objectives is to optimize the usage of carbon fibers along with health monitoring of COPVs, this task focused on quantifying the strength translation of carbon fibers, first using coupons and second by using standard test and evaluation bottles (STEBs).

ORNL fabricated unidirectional flat panels using the filament winding method on a flat paddle mandrel as shown in Figure 6. The panels used ITS50-24K carbon fiber towpregs provided by Teijin Carbon America (Figure 7). The winding and consolidation/curing conditions were selected in order to match as closely as possible the cylinder production parameters when producing the test panels. The winding advance for the panels was set at 4 mm/revolution (0.157 in/rev) in order to match the nominal towpreg width and anticipated nominal advance to be used in test tank production. Targeted panel thickness was about 1 mm (0.040 in) for fiber-directional test coupons and about 2 mm (0.080 in) for transverse-directional testing. To attain these thicknesses, 3 passes (1-1/2 complete circuits) were utilized for the 1 mm panels and 6 passes (3 complete circuits) were utilized for the 2mm panels. The panels were wound at room temperature, which was about 18 ^{o}C (65 ^{o}F) in the laboratory at the time the panels were produced. The panels were wound with about 67 N (15 lbs.) tow tension without wiping, scraping, or other consolidation aids employed. After winding, the panels (on the mandrel) were transported to a laboratory press for cure at relatively low pressure. The panels were sandwiched between mold-released aluminum caul plates and pressurized to 2 tons, representing less than 15 lbs. per square inch. Temperature was ramped to 85 ^{o}C (185 ^{o}F) and held for 1 hour and then ramped to 149 ^{o}C (300 ^{o}F) for another 1 hour dwell. After curing, the press and panel were allowed to gradually cool to room temperature overnight before being cut and removed from the mandrel for testing. Panels labeled as SH2 A and B were the two sides of the 1 mm fabrication while SH3 A and B were from the 2 mm fabrication. The processing parameters are summarized in Table 1.

TABLE 1: SUMMARY OF PROCESS DETAILS IN FABRICATION OF THE FLAT PANELS OF ITS50-24K

Towpreg: :	TCR- Spool 1, 4mm ITS-50 F23-24K UF3369-100
Tension:	44.5 N (10 lbs)
Fiber Advance:	Start with 0.157 in/rev (@.65 fiber volume, thickness should be about .0144in per layer)
# layers or passes:	3 (1-1/2 complete "circuits")
Wiping:	None
Winding Temps:	RT (measure and record)
Gelation:	NA
Press:	Mold release caul plates, pressurize to ~2 tons (~25 psi) and ramp to 215 ^{o}F at 5 ^{o}F/min. Hold for 1 hour. Increase pressure to 5 tons (~70 psi) and ramp to 285 ^{o}F at 5 ^{o}F/min. Hold for 1 hour. Release pressure and cool in press 1 hour minimum.

FIGURE 6: FLAT PANELS OF UNIDIRECTIONAL COMPOSITE FABRICATED BY ORNL USING FILAMENT WINDING ON A FLAT PADDLE

FIGURE 7: TOWPREGS WITH ITS50-24K CARBON FIBER SUPPLIED BY TEIJIN CARBON AMERICA

ORNL performed compositional testing using the microwave-powered digestion technique as specified in ASTM D3171 Procedure F—Matrix Digestion With Nitric Acid In A Microwave Oven. Considering the lack of prior winding trials with this towpreg material and no previous experience with this material system to tweak the fiber and resin constituent data used in the composition testing analysis, the data as shown in Table 2 indicates relatively consistent fiber volumes for most samples: between 60.7% and 61.9% (one individual sample was actually 59.6%) and void fractions between 0.6% and 1.6%. As has been our previous experience in winding test panels, these panels were found to have slight warpage thought to be a function of the tension gradient created in winding around a flat surface; use of the small amount of pressure in curing probably helps mitigate this warpage and somewhat simulate the natural consolidation that is created in winding over a round surface with fiber tension.

Coupons prepared from laminate were tested for material orthotropic properties to be used in finite element analysis. First the fiber orientation in the panels was verified by optical microscopy. The volume fraction of the composite laminate was verified by thermo-gravimetric analysis (TGA). Subsequently, mechanical tensile tests were performed according to ASTM D3039. The test results are summarized in Table 2.

TABLE 2: SUMMARY OF TEST RESULTS FROM COUPON TESTING

Specimen ID	Panel Source	Laminate Density	Fiber Density	Resin Density	Fiber Welght Fraction	Resin Weight Fraction	Fiber Volume Fraction	Resin Volume Fraction	Void Fraction
		g/cc	g/cc	g/cc	%	%	%	%	%
1	SH3B 1	1.5510	1.8	1.18	71.43	28.57	61.5	37.6	0.9
2	SH3B3	1.5381	1.8	1.18	71.20	28.80	60.8	37.5	1.6
3	SH2B 1	1.5553	1.8	1.18	71.66	28.34	61.9	37.4	0.7
4	SH2B 3	1.5454	1.8	1.18	71.97	28.03	61.8	36.7	1.5
5	SH3A 3	1.5447	1.8	1.18	71.70	28.30	61.5	37.0	1.4
6	SH3A 1	1.5336	1.8	1.18	69.95	30.05	59.6	39.1	1.4
7	SH2A 3	1.5405	1.8	1.18	70.92	29.08	60.7	38.0	1.3
8	SH2A 1	1.5494	1.8	1.18	70.50	29.50	60.7	38.7	0.6

Samples were tested according to ASTM D3039 for mechanical properties parallel and perpendicular to the carbon fiber orientation. An MTS 813 (Model 318.10; MTS Systems Corporation) testing platform with pneumatic grips was used to perform the mechanical tests. A constant crosshead speed of 2 mm/min was used to deform the samples, and tensile strain was measured with an MTS 634.11E-25 strain gage (MTS Systems Corporation). Furthermore, all samples were tabbed with a glass-fiber-reinforced thermoplastic composite to ensure the samples did not slip in the grips. Five samples from each plate were used to obtain averaged properties.

Figure 8(a) and (b) compare the fiber- and transverse-direction tensile modulus from the plate pairs as well as the distribution of individual sample values and their respective failure modes. Good agreement is found between the corresponding plate pairs. However, it is noted that half of the fiber-direction samples did experience a splitting failure mode as opposed to the expected explosive failure mode. Figure 9(a) and (b) compare the fiber- and transverse-direction strength from the plate pairs as well as the distribution of individual sample values and their respective failure modes. Here, the “B-side” samples are found to have a systematically higher tensile strength than the “A-side” samples. Precisely why this is the case is not understood. Finally, Table 3 lists the average values and standard deviations of the tensile moduli and strengths measured in this work.

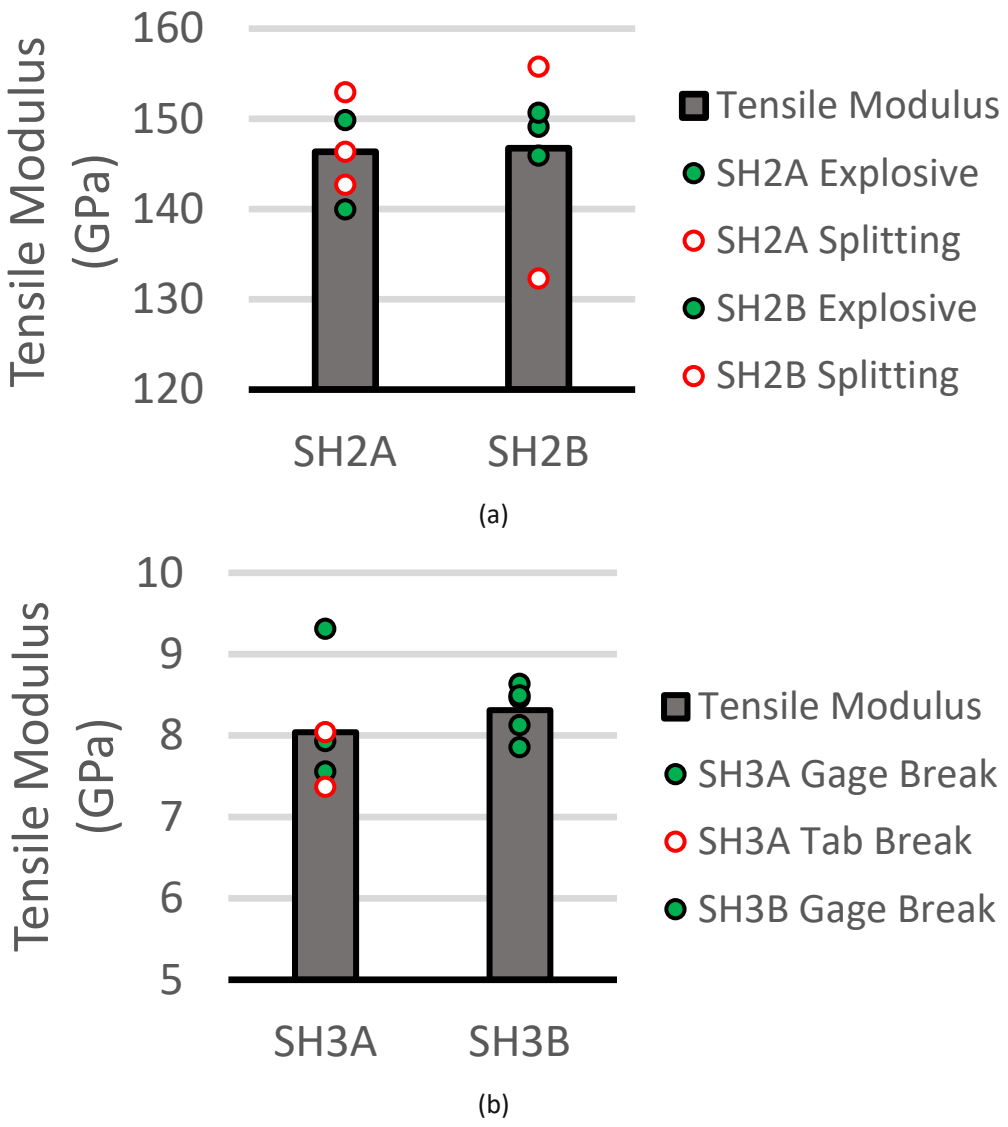

FIGURE 8: AVERAGED AND INDIVIDUAL TENSILE MODULUS VALUES FOR THE FIBER-DIRECTION (A) AND TRANSVERSE-DIRECTION (B) PLATES. NOTE THAT THE COLOR OF THE INDIVIDUAL SAMPLE MARKER DENOTES THE FAILURE MODE OF THE SAMPLE

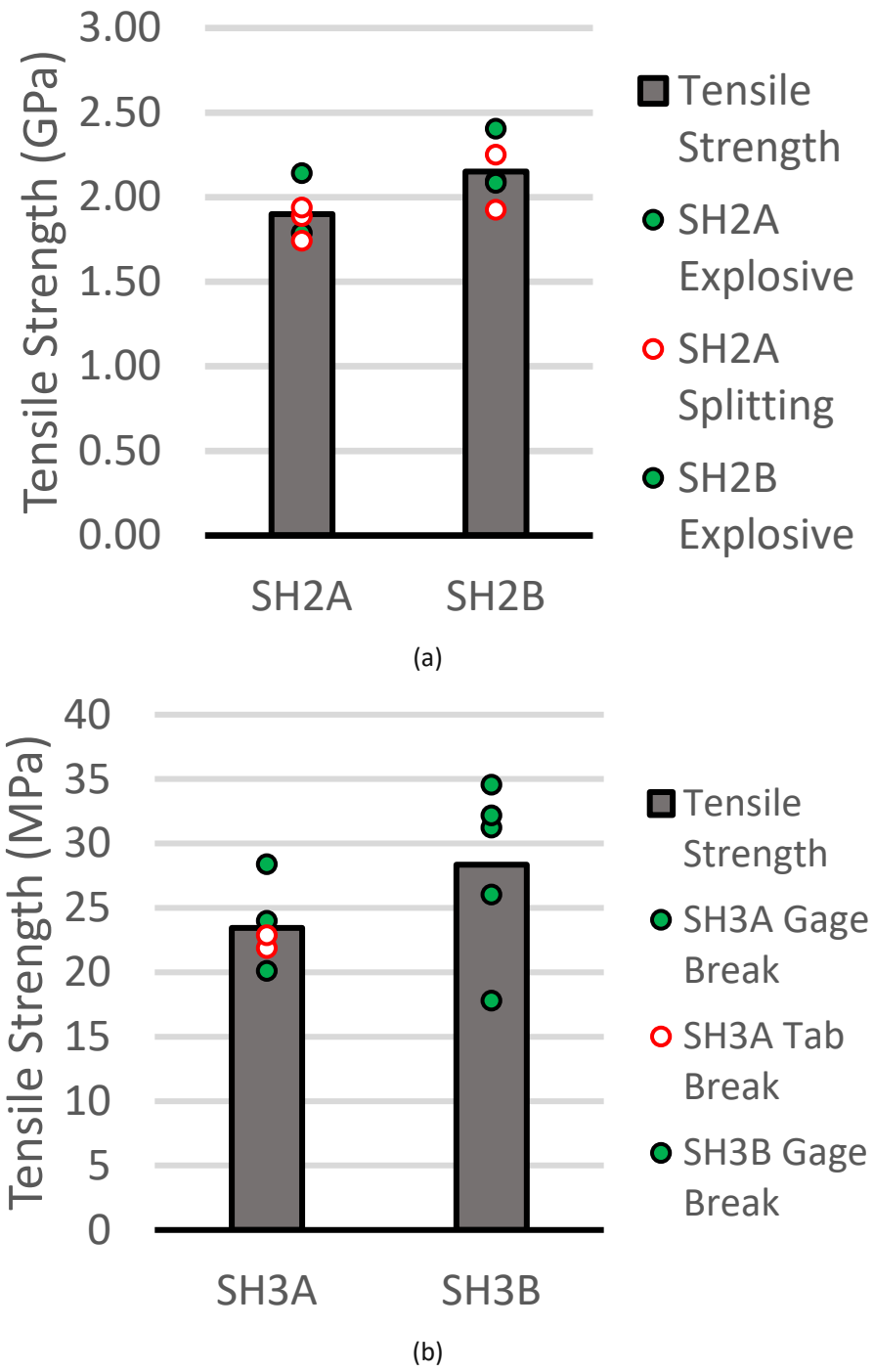

FIGURE 9: AVERAGED AND INDIVIDUAL TENSILE STRENGTH VALUES FOR THE FIBER-DIRECTION (A) AND TRANSVERSE-DIRECTION (B) PLATES. NOTE THAT THE COLOR OF THE INDIVIDUAL SAMPLE MARKER DENOTES THE FAILURE MODE OF THE SAMPLE

TABLE 3: AVERAGED VALUES AND STANDARD DEVIATION OF TENSILE PROPERTIES FROM THE FOUR PLATES

		Modulus (GPa)		Strength (GPa)	
		Average	*Standard Deviation*	*Average*	*Standard Deviation*
Fiber Direction	A	146	5.24	1.89	0.156
	B	147	8.83	2.19	0.182
Transverse Direction	A	8.04	0.759	0.0234	0.00311
	B	8.31	0.316	0.0284	0.00667

Fiber orientation within the laminates was verified qualitatively by optical microscopy. Microscopy samples were cut from the plates separately from the tensile test samples using a diamond saw. These were then potted in epoxy and sanded and polished in preparation for taking micrographs. Micrographs were taken at 10x and 150x magnification, and representative images are shown in Figure 10(a)-(d). These show little evidence of fiber misalignment.

Fiber content was verified by both acid digestion conducted at ORNL and TGA conducted at UTK. Fiber content from TGA was measured in a Pyris 1 (PerkinElmer) using a nitrogen atmosphere to prevent fiber oxidation. Measurements come from two 10 mg samples taken from each plate, separate from the mechanical testing coupons. Figure 11 shows the mass loss during the temperature ramp. In all cases, fiber loading is near its target of 73% by mass.

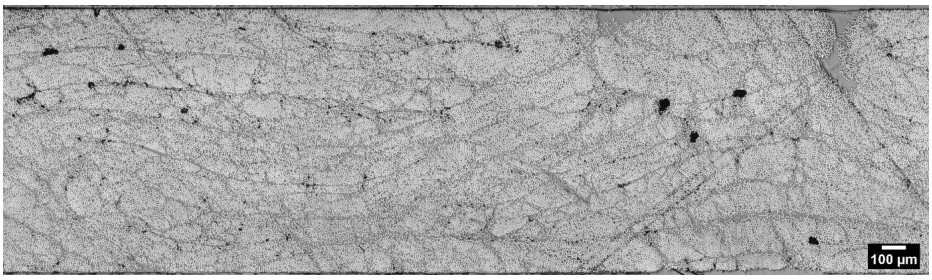

(a)

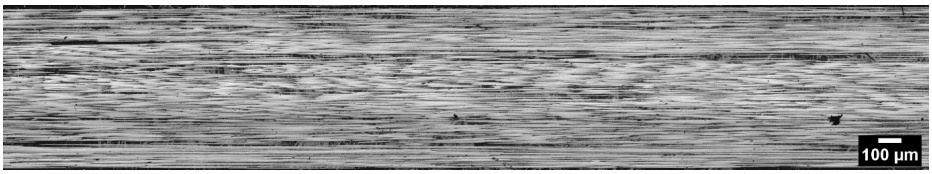

(b)

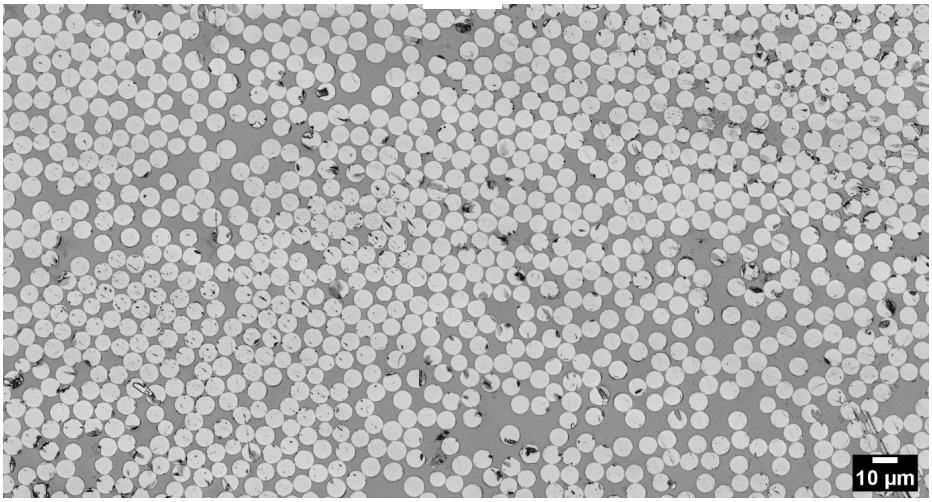

(c)

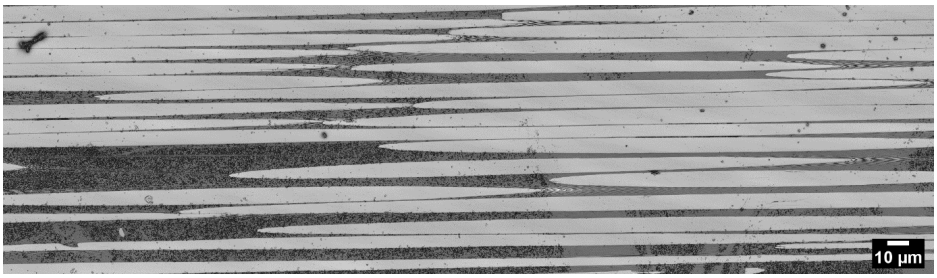

(d)

FIGURE 10: REPRESENTATIVE MICROGRAPHS USED TO QUALITATIVELY VERIFY FIBER ORIENTATION IN THE LAMINATE PANELS. ALL MICROGRAPHS ARE TAKEN FROM PANEL SH2B. PICTURES (A) AND (B) ARE THE TAKEN PARALLEL AND PERPENDICULAR TO THE FIBER DIRECTION, RESPECTIVELY, AT 10X MAGNIFICATION. PICTURES (C) AND (D) ARE TAKEN PARALLEL AND PERPENDICULAR TO THE FIBER DIRECTION, RESPECTIVELY, AT 150X MAGNIFICATION

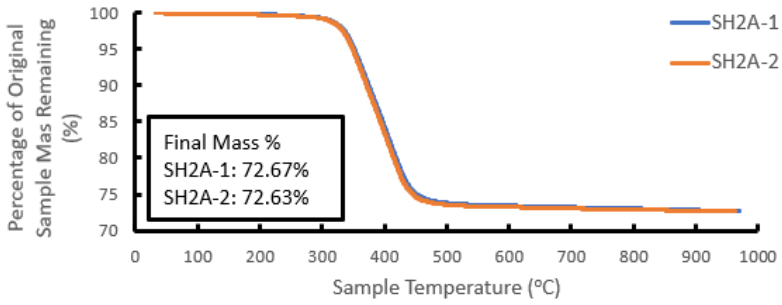

(a)

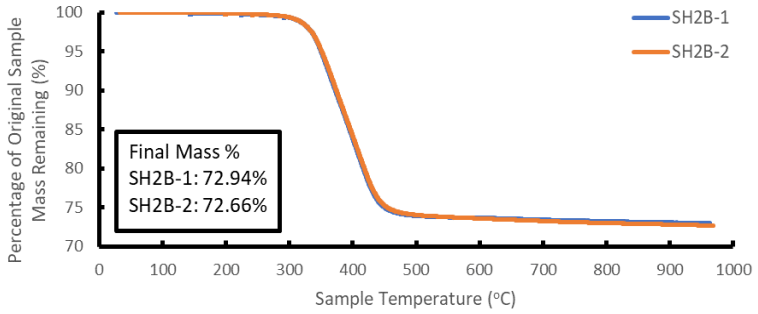

(b)

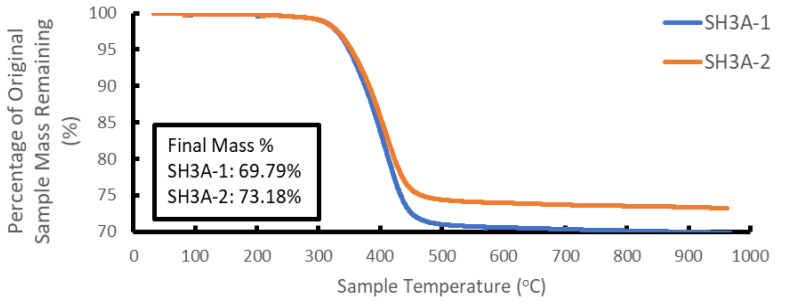

(c)

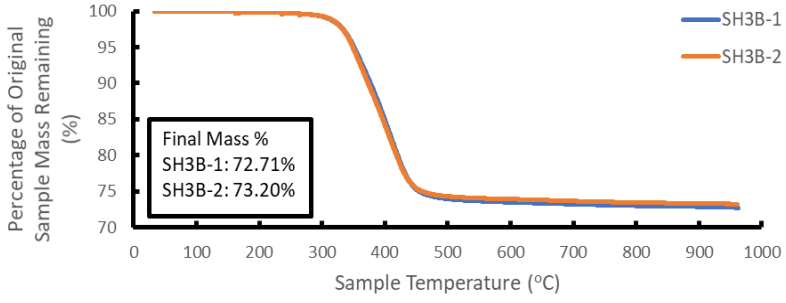

(d)

FIGURE 11: MASS LOSS CURVES FROM TGA FOR SAMPLES FROM EACH PLATE USED IN THE TENSILE TESTING

Subsequent to coupon testing, 150 mm (6 in. dia.) x 460 mm (18 in.) long standard test and evaluation bottles (STEBs) were fabricated by filament winding ITS50-24K towpreg over Aluminum liners. The composite overwrap in the STEB consists of 2 helicals and 2 hoop plies. The material properties of the composite plies determined in coupon testing were used to ensure that the failure mode in STEB is due to hoop stresses in the cylindrical section. The rupture mode of the STEB validated this design projection (Figure 12). Five (5) STEBs were fabricated altogether in the exact same way and burst tested. The burst results are summarized in Figure 13. The test results show good, consistent performance of ITS50-24K fiber within the allowable manufacturing variation.

FIGURE 12: CYLINDRICAL BURST MODE IN A STEB VESSEL SUBJECTED TO A HYDROSTATIC BURST TEST

After the completion of burst test evaluation of STEBs, two more STEBs were manufactured to investigate the use of high-definition distributed fiber optic sensors (HD-DFOSs) for structural health monitoring (SHM). A wide variety of techniques are available for SHM, and HD-DFOSs are particularly interesting for their ability to measure strain along the entire length of the sensor, as opposed to strain measurements at discrete locations as with fiber Bragg grating (FBG) sensors. This is particularly intriguing for early detection of damage, which can occur at random locations. The HD-DFOS can also be embedded within composite laminates, or even tows of reinforcing fiber, to provide a detailed picture of the strains throughout the composite laminate.

Both STEBs were made with an aluminum liner and four layers of the same towpreg used in the composite coupon testing. Table 4 lists the winding schedule used for both vessels. One vessel was equipped with four HD-DFOSs (LUNA Innovations) to measure strains during winding, autofrettage, and pressurization. Three of these sensors were embedded within the composite overwrap at the interfaces of the liner and first wrap, the first and second wraps, and the second and third wraps. A HD-DFOS was placed on the outer surface of this vessel as well. The

TABLE 4: WINDING SCHEDULE FOR THE STEBS USED IN THIS WORK.
ANGLES ARE MEASURED FROM THE AXIS OF THE VESSEL

Layer	Winding Angle
Sensor (Vessel 1)	
1	89°
Sensor (Vessel 1)	
2	+/- 15°
Sensor (Vessel 1)	
3	+/- 15°
4	89°
Sensor (Both Vessels)	

second vessel was used for burst testing, and a single HD-DFOS sensor was placed on the surface of this vessel.

Figure 14 and Figure 15 show the paths of the HD-DFOSs as planned for integration in a STEB. The path shown in Figure 14 was chosen to give a full picture of the strain state, to include strains in the hoop and axial directions, as well as the strains in the direction of the helix wraps. A template was made to assist in accurately placing the fiber (Figure 16(a)). The path in Figure 15 was chosen with the goal of detecting damage within the composite overwrap and only looks at strains along the hoop and axial direction. In both cases, strain measurements were limited to the cylindrical section of the vessels. Strain was measured in both vessels using an ODiSI 6 interrogator (LUNA Innovations) with remote modules (Figure 16 (b)). All of the vessels in this study were wound using a McClean-Anderson Spider. Figure 17 shows the STEB after winding.

SN	Burst pressure (psi)
3317	6863
3443	7550
3451	6795
3452	6889
3457	6418
SUM	34515
AVG	6903

FIGURE 13: BURST TEST PICTURES OF STEBS FABRICATED WITH TEIJIN ITS5-24K AND A SUMMARY OF BURST TEST RESULTS

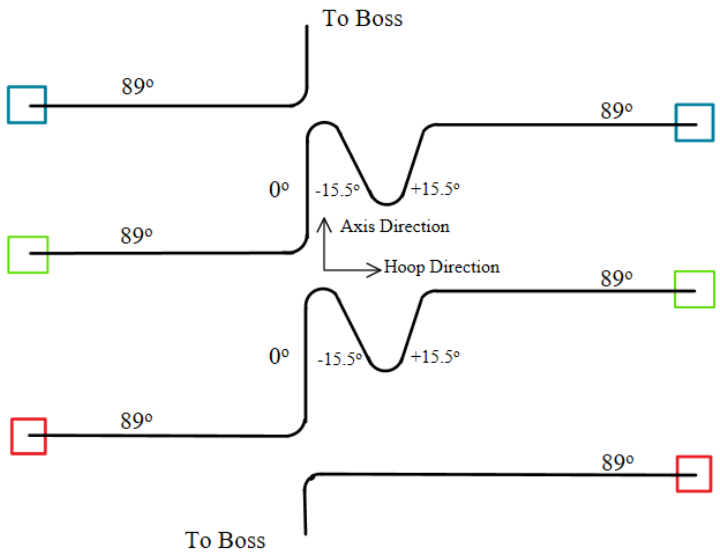

FIGURE 14: SCHEMATIC OF THE HD-DFOS PATH ON THE VESSEL WITH EMBEDDED SENSORS. MEASUREMENTS WERE LIMITED TO THE CYLINDRICAL SECTION OF THE VESSEL

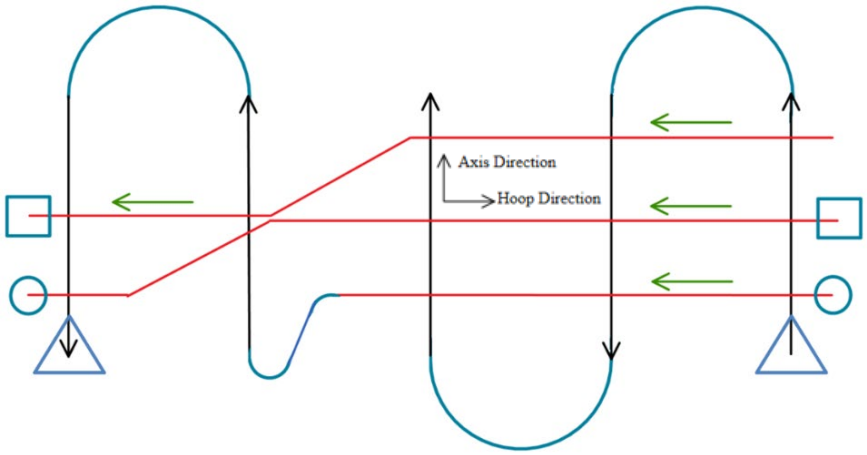

FIGURE 15: SCHEMATIC OF THE HD-DFOS PATH ON THE SURFACE OF THE VESSEL USED IN BURST TESTING. THE AXIS-ORIENTED SEGMENTS (BLACK) WERE LAID ON THE SENSOR FIRST, AND THE HOOP-ORIENTED SEGMENTS (RED) WERE LAID ON TOP OF THEM. THIS DID RESULT IN SHORT REGIONS IN WHICH THE HOOP-ORIENTED SEGMENTS WERE NOT BOUND TO THE VESSEL SURFACE, AND THIS IS OBSERVED IN THE STRAIN PROFILES. MEASUREMENTS WERE LIMITED TO THE CYLINDRICAL SECTION OF THE VESSEL

(a) (b)

FIGURE 16: (A) APPLICATION OF FIBER OPTIC SENSORS (FOS) DURING FABRICATION OF A STEB AND (B) LUNA'S DATA ACQUISITION SYSTEM USED FOR SENSOR INTERROGATION DURING PRESSURE TESTING OF STEB

FIGURE 17: STEB WITH FIBER OPTIC SENSORS AT THE END OF FABRICATION

Monitoring of strains in the composite overwrap accrued during manufacturing is of additional interest, as they influence the performance of the vessel when in service. Figure 18 plots the strain profile of each of the three HD-DFOSs embedded within the composite overwrap after winding the STEB, but before curing the resin. The plot indicates that the liner has not changed shape after winding. Some compression is observed in the hoop direction, but this is very small relative to hoop strains within the overwrap. Compression in the hoop direction increases in magnitude with increasing distance from the liner. Conversely, tension is observed in the axial and helical directions. The strain profiles show that the liner essentially retains its shape, so the forces applied during winding are not strong enough to plastically deform it. Compression in the hoop direction, and the corresponding tension in the axis direction, suggests good contact between the overwrap and the liner. The point-by-point fluctuations observed in the profiles are common to all strain profiles measured in all of the pressure vessels used in this project and are addressed later.

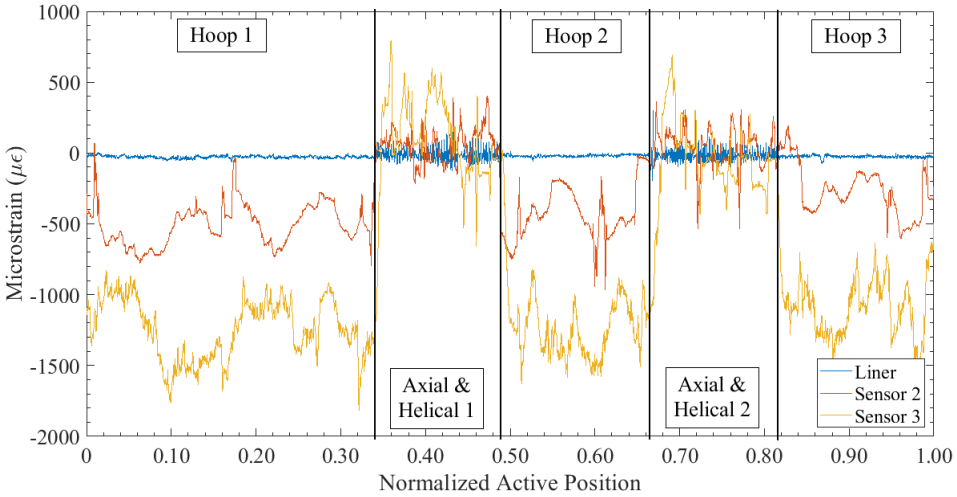

FIGURE 18: STRAIN PROFILES MEASURED BY THE EMBEDDED HD-DFOSS AFTER WINDING THE STEB DESIGNATED FOR PRESSURIZATION. "NORMALIZED ACTIVE POSITION" IS CALCULATED BY ISOLATING THE LENGTH OF THE HD-DFOS BOUND TO THE CYLINDRICAL PORTION OF THE VESSEL AND NORMALIZING THE POSITION ON THE HD-DFOS AGAINST THIS LENGTH. MATHEMATICALLY: $NAP = (P - P_0)/(P_L - P_0)$ WHERE P_0 AND P_L DENOTE THE BEGINNING AND END OF THE SEGMENT OF THE HD-DFOS BOUND TO THE CYLINDRICAL PORTION OF THE VESSEL, RESPECTIVELY

Figure 19 plots the strain profiles measured by all four sensors after the vessel was cured. During the curing process, the liner expands while the overwrap shrinks due to carbon fiber's negative coefficient of thermal expansion in the fiber direction. Once the resin has cured, those strains are "baked" into the vessel, hence the residual tensile hoop strain in the liner alongside the compressive hoop strain. The compressive axial and helical strains in the overwrap likely arise from the shrinking induced by the helical wraps.

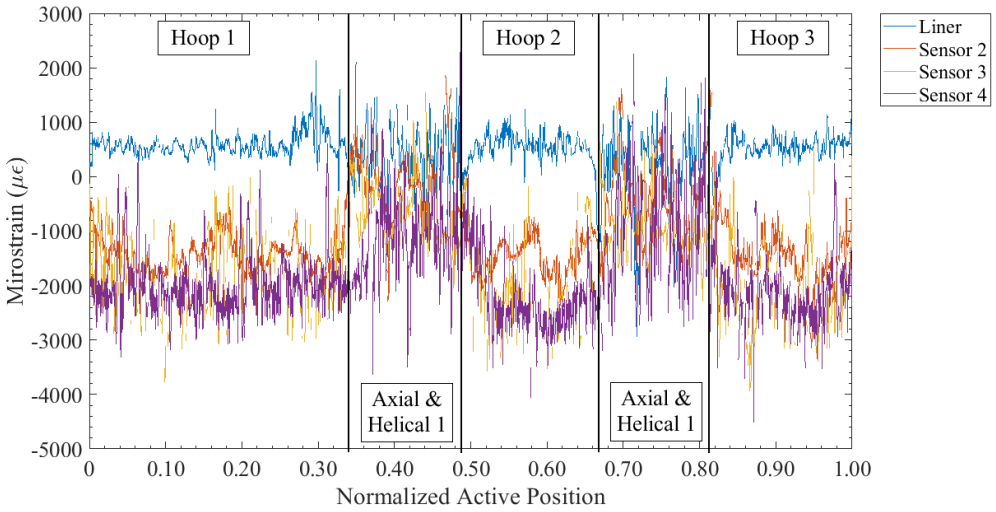

FIGURE 19: STRAIN PROFILES MEASURED BY THE EMBEDDED HD-DFOSS AFTER CURING THE STEB DESIGNATED FOR PRESSURIZATION. "NORMALIZED ACTIVE POSITION" IS CALCULATED BY ISOLATING THE LENGTH OF THE HD-DFOS BOUND TO THE CYLINDRICAL PORTION OF THE VESSEL AND NORMALIZING THE POSITION ON THE HD-DFOS AGAINST THIS LENGTH. MATHEMATICALLY: $NAL = (P - P_0)/(P_L - P_0)$ WHERE P_0 AND P_L DENOTE THE BEGINNING AND END OF THE SEGMENT OF THE HD-DFOS BOUND TO THE CYLINDRICAL PORTION OF THE VESSEL, RESPECTIVELY

Once the STEB was wound and cured, it was filled with automatic transmission fluid, placed in a testing chamber with blast doors, and connected to a pressurization unit for autofrettage and step pressurization (Figure 20). After the vessel with embedded sensors was autofrettaged, it was pressurized in steps from 500 psig to 3,000 psig in increments of 500 psig. Excellent correlation was observed between the fiber optic sensor data and the mechanical strain gages on the outermost layer of the vessel (Figure 21).

FIGURE 20: PRESSURIZATION CHAMBER WITH RAISED BLAST DOORS

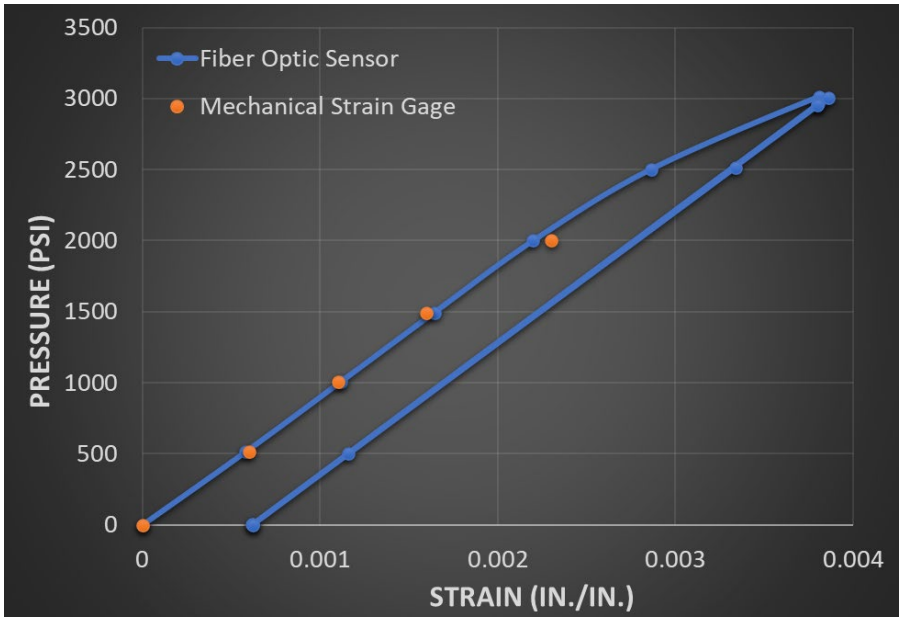

FIGURE 21: CORRELATION OF FOS AND MECHANICAL STRAIN GAGE PLOT OF PRESSURE VS STRAIN AS DETERMINED FROM HYDROSTATIC PRESSURIZATION OF A STEB

Figure 22, Figure 23 and Figure 24 plot the strain profiles through the overwrap thickness at pressure levels of 69 barg, 139 barg and 207 barg (1,000 psig, 2,000 psig, and 3,000 psig), respectively. All strains increase as internal pressure increases, as expected. Moreover, the hoop strains grow at a much faster rate than the axial and helical strains, indicating that the vessel expands circumferentially, but not axially. There is also very little difference between the strains at the different layers in the composite overwrap, suggesting that a single surface-mounted sensor might be sufficient for tracking the mechanical performance of the composite overwrap.

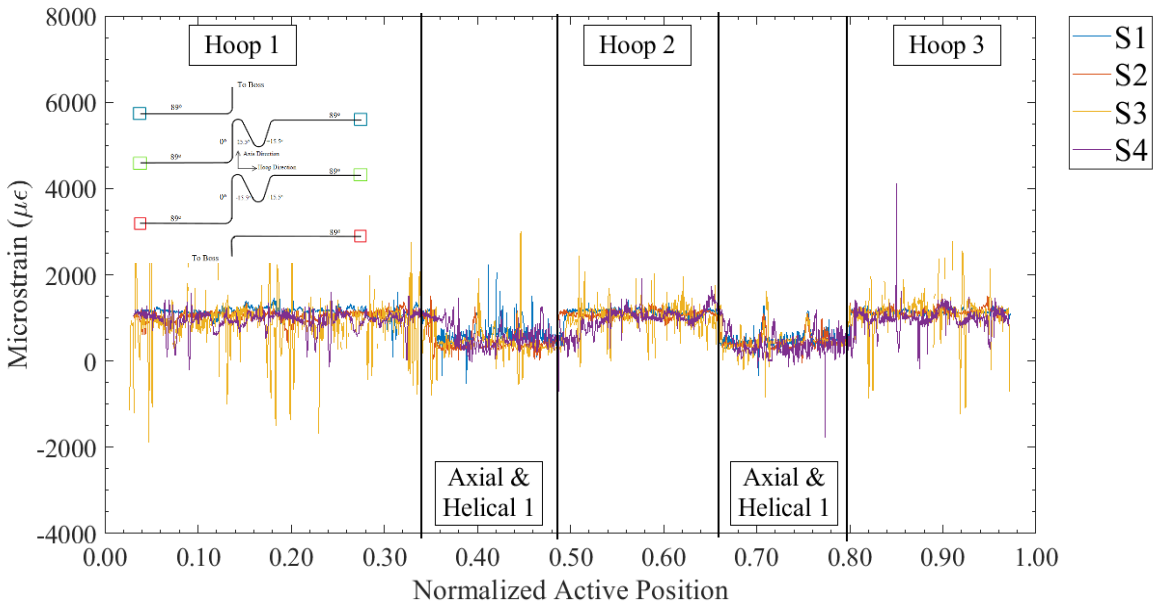

FIGURE 22: STRAIN MEASURED BY THE EMBEDDED HD-DFOSS AT 69 BARG (1,000 PSIG). SENSOR 1 (S1) IS ON THE LINER, SENSOR 2 IS LOCATED BETWEEN THE FIRST HOOP WRAP AND THE FIRST HELICAL WRAP, SENSOR 3 (S3) IS AT THE INTERFACE BETWEEN THE TWO HELICAL WRAPS, AND SENSOR 4 (S4) IS ON THE VESSEL SURFACE

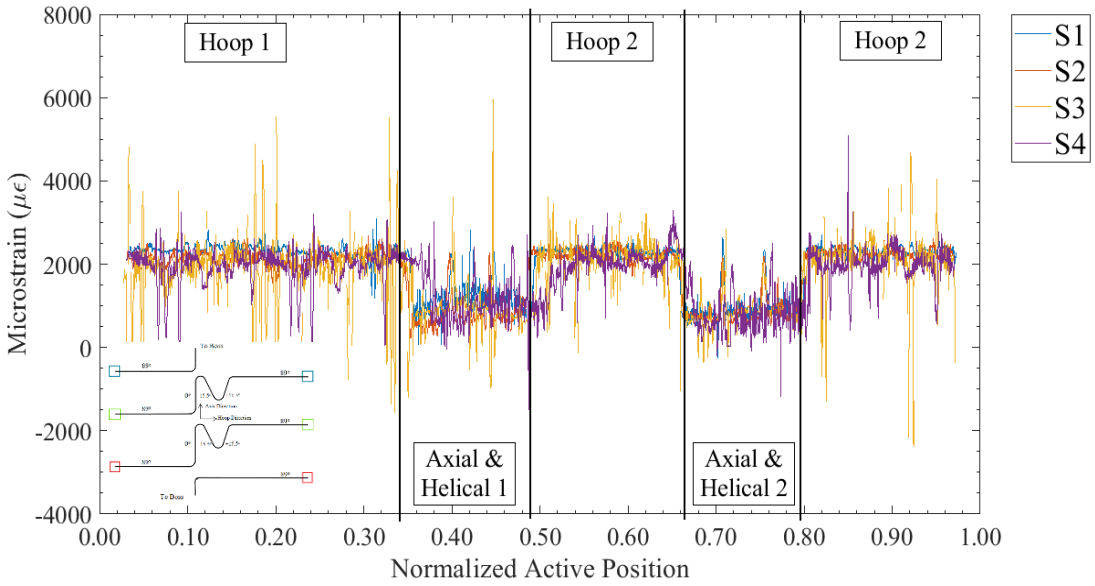

FIGURE 23: STRAIN MEASURED BY THE EMBEDDED HD-DFOSS AT 139 BARG (2,000 PSIG). SENSOR 1 (S1) IS ON THE LINER, SENSOR 2 IS LOCATED BETWEEN THE FIRST HOOP WRAP AND THE FIRST HELICAL WRAP, SENSOR 3 (S3) IS AT THE INTERFACE BETWEEN THE TWO HELICAL WRAPS, AND SENSOR 4 (S4) IS ON THE VESSEL SURFACE

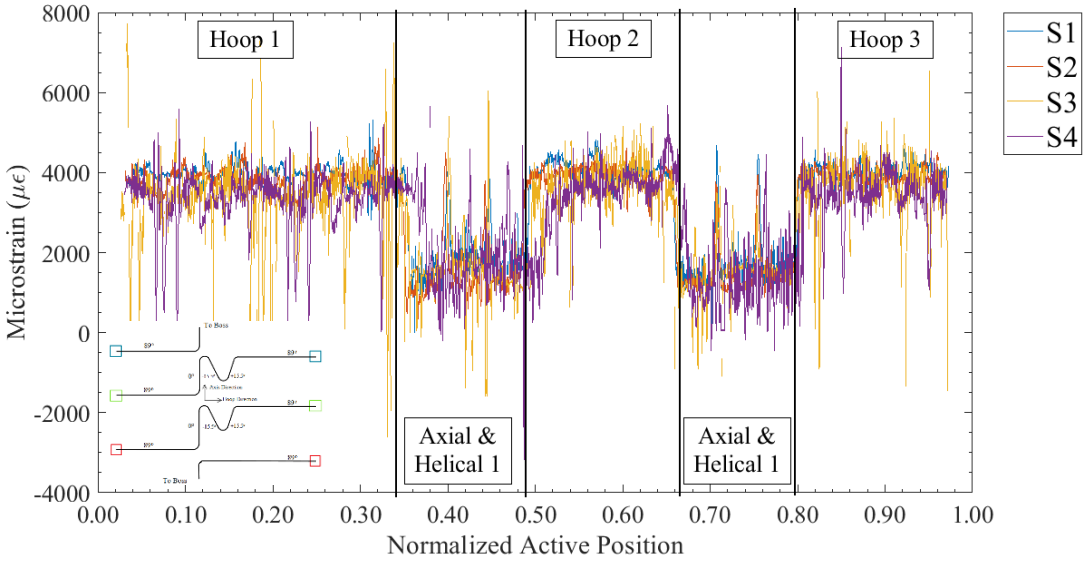

FIGURE 24: STRAIN MEASURED BY THE EMBEDDED HD-DFOSS AT 207 BARG (3,000 PSIG). SENSOR 1 (S1) IS ON THE LINER, SENSOR 2 IS LOCATED BETWEEN THE FIRST HOOP WRAP AND THE FIRST HELICAL WRAP, SENSOR 3 (S3) IS AT THE INTERFACE BETWEEN THE TWO HELICAL WRAPS, AND SENSOR 4 (S4) IS ON THE VESSEL SURFACE

Point-by-point fluctuations in strain also appear to get much larger as pressure increases. Initially, one is tempted to dismiss this fluctuation as random noise, however, the specific locations of the peaks and troughs in the profiles remain the same as internal pressure increases. If the point-by-point fluctuations were indeed noise, peaks and troughs in the profile would constantly change location. These fluctuations then suggest that strains are not uniform throughout the laminate, as is commonly assumed. Furthermore, when these fluctuations are averaged out, they agree with mechanical strain measurements. Figure 25 compares strain measurements from a resistive strain gage placed near the middle hoop segment of the HD-DFOS, and the strain measured by the HD-DFOS averaged along the middle hoop section. Both measurements are in reasonable agreement, and both follow a similar trend with increasing internal pressure.

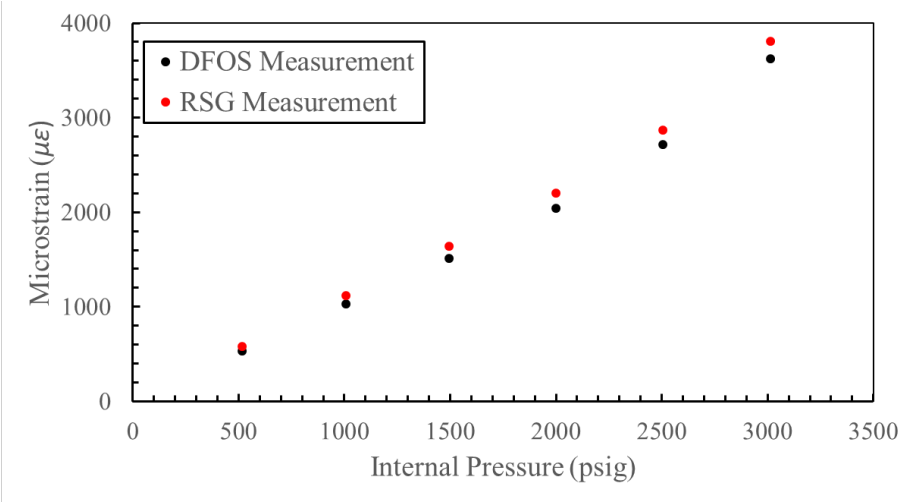

FIGURE 25: COMPARISON BETWEEN STRAINS MEASURED BY A RESISTIVE STRAIN GAGE (RSG) AND THE AVERAGE OF THE STRAIN MEASURED BY THE DISTRIBUTED FIBER OPTIC SENSOR (DFOS) ALONG THE MIDDLE HOOP SEGMENT (HOOP 2)

Based on the results from the first STEB, a second STEB was made to be outfitted with a single, surface-mounted HD-DFOS to measure the strain as the vessel was pressurized to burst. Before the HD-DFOS was bound to the surface of the composite overwrap, the overwrap surface was sanded to be relatively smoother. Because the HD-DFOS winds over itself, the hoop- and helical-direction segments lie on top of the axis-oriented segments. It was assumed that this would have minimal impact on the strain readings, however, it led to distinct peaks in the strain measurements that corresponded to the intersection points and prevented the HD-DFOS from bonding to the composite overwrap at some points. Once the STEB was made and the HD-DFOS was bound to the surface, it was filled with water, taken to the burst testing pit, and hooked up to a pressurization unit.

Figure 26 shows the resulting residual strains in the STEB used in the burst test. The hoop segments are indeed under tension on the surface of the composite overwrap and based on the results from the STEB with embedded HD-DFOSs, this should hold throughout the composite overwrap thickness. The axial segments are comparatively neutral; however, one end of the composite overwrap appears to be under compression. It is conjectured that this is caused by the shoulder region of the composite overwrap, where the overall composite thickness becomes higher due to dwell in the filament winding process.

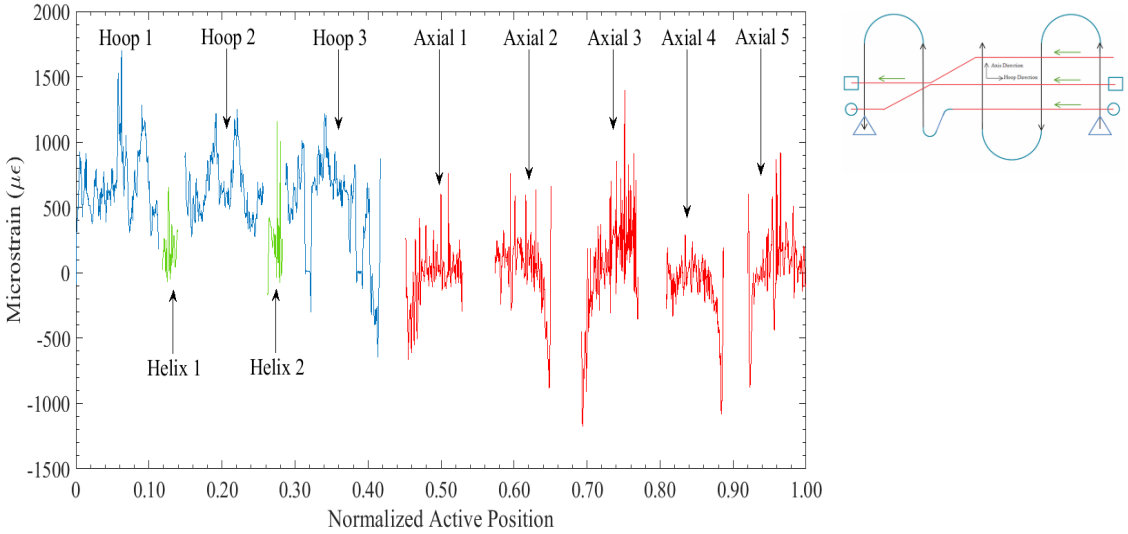

FIGURE 26: RESIDUAL STRAINS INDUCED BY AUTOFRETTAGE IN THE STEB USED IN BURST TESTING

One important implication of the non-random point-by-point fluctuations in the strain profile is that the peaks are potential points for localized failure within the composite overwrap. If these points correlate with actual failure locations within the composite overwrap, then a structural health monitoring algorithm could be designed to monitor these points and alert an operator to early signs of vessel failure, well before damage has progressed too far for an intervention. With this in mind, strain measurements were taken throughout the burst test as the vessel was pressurized.

Figure 27 shows the strain profile as a function of increasing pressure. As in the STEB with embedded HD-DFOSs, the profile maintains its shape with increasing pressure, and the peaks and troughs in the profile become more pronounced. However, there is no obvious location along the profile where strain grows at a conspicuously faster rate than surrounding points. The final profile actually shows the HD-DFOS signatures breaking, which was a consequence of wrapping the hoop-oriented segments on top of the axis-oriented segments. However, the vessel burst shortly after the HD-DFOS signature stopped recording. Therefore, this would not have been a useful early warning system even if the HD-DFOS had survived throughout the test. Later tests with a full-size vessel showed

similar results with a HD-DFOS that survived up to the vessel burst. These strain readings suggest that the composite overwrap ruptures very rapidly, and failure in an undamaged vessel would be very difficult to track, at least with a surface mounted sensor.

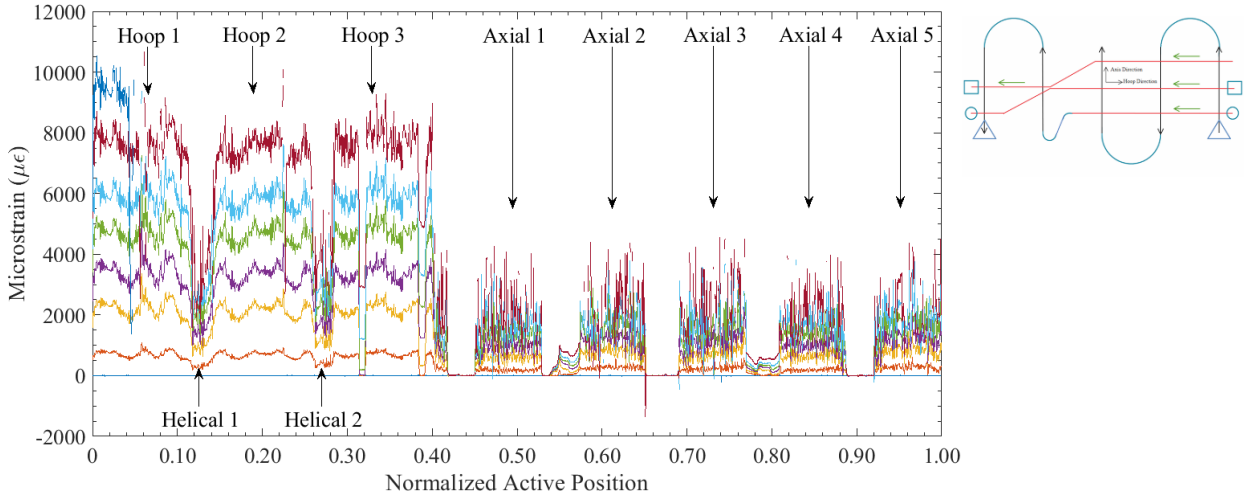

FIGURE 27: BURST STEP STRAIN GROWTH DURING PRESSURIZATION

All of the previous work was performed on pristine, as-fabricated STEB vessels. It is expected that composite vessels in actual service will accumulate damage over their service life. This damage, as it grows, can alter the mechanical performance of the composite overwrap, potentially inducing premature failure. One particular form of damage is delamination, which can be induced by even low energy impacts (~5 J). This is equivalent to dropping a 3.6 kgs (8 lbs.) mass (say a wrench) from a height of only 140 mm (5.5 in.). Because this type of damage can occur randomly, strain sensors set up for measurements at discrete points can miss it until the damage grows too large for an intervention. Moreover, these low energy impacts leave little, if any, outward evidence of damage and could pass a visual inspection, while significant subsurface delamination remains in the vicinity of the impact site.

To investigate the ability of the HD-DFOSs to capture low velocity impact damage, a STEB with embedded sensors was impacted at the same location at increasingly higher impact energies. This was performed with a Gardner impact testing platform by dropping an 3.6 kgs (8 lbs.) mass through a guide tube and striking a tup (falling weight) with 12.5 mm (0.5 in.) diameter hemispherical end (Figure 28). Strain measurements from the HD-DFOS were supplemented with fiber Bragg grating sensors (FBGs) and digital image correlation (DIC). Two FBGs with 10 mm gage lengths were supplied by LUNA Innovations (formerly a product of Micron Optics), and these were used with a HYPERION si155 interrogator. The FBGs were included because they can acquire data at much faster rates than the HD-DFOSs. The slower acquisition rate of the HD-DFOSs is, in fact, a direct consequence of their high spatial resolution, and measurements will not register during the impact. Strain data during impact will provide data that can be used to refine FEA modeling. One sensor was placed adjacent to the impact site, and one sensor was placed directly opposite the impact site on the vessel's underside.

The DIC was performed using cameras and UV lights from GOM measurement system and data was analyzed with Aramis Professional 2018. Strain measurements from DIC were used to determine how widespread the impact damage was. Another shortcoming of the HD-DFOSs is that they can only measure strain at the location to which they are bound. It can be difficult to gauge the true extent of a damaged area without a laydown path designed specifically for this purpose (e.g. winding the HD-DFOS in a helical pattern around the vessel). The DIC offers a wider field of view that can supplement the highly localized HD-DFOS measurements.

FIGURE 28: IMPACT TESTING SETUP

Stress rupture failure is a major point of concern for pressure vessels. This occurs when a seemingly healthy vessel bursts as it is pressurized to a pressure below its expected burst pressure. This burst often occurs due to the slow growth of cracks or delaminations within the overwrap over time. Ideally, this would be evaluated through pressure cycling. Strain profiles from embedded HD-DFOSs measured before and after a representative number of cycles could hypothetically change, indicating the growth of damage within the overwrap and serving as an early warning system for vessel health. The highly localized strain measurements of the HD-DFOS are well-suited to this end, as cracks and delaminations tend to be highly localized as well. For various reasons, pressure cycling was never successfully performed on vessels with embedded sensors.

Low-velocity impacts are another source of damage within the pressure vessel overwrap. Many times, these lead to barely visible impact damage (BVID). In these cases, there is very little change in the surface topography and extensive delamination under the surface. Low-velocity impacts tend to be random one-off events. However, multiple impacts could be leveraged to evaluate the ability of the HD-DFOSs to detect damage propagation in place of more traditional pressure cycling

There was no significant shift recorded in the response from mechanical strain gages and the DFOS embedded in the STEB vessel due to fatigue effect when the vessel was subjected to 1,000 pressure cycles up to its maximum expected operating pressure (MEOP). This is not unexpected since the Tension-Tension fatigue S-N curves for continuous carbon fiber composites are relatively flat and loading the composite shell to design allowable stress levels results in infinite life.

However, the program team believes that the damage propagation mechanism under pressure cycles is critical for vessel safety and this is an area where embedded DFOS can help with detection.[5] Therefore, repeated impacts were used in a revised experimental setup in place of the fatigue testing to evaluate damage propagation. Impact energy started at 5 J and ramped up to 10 J in 1 J increments, for a total of 6 impacts at the same location, using a 3.6 kgs (8 lbs.) mass. During the test setup, the surface-mounted HD-DFOS stopped working, so data was only collected from the three HD-DFOSs embedded in the composite overwrap. The gratings in the FBG were placed

[5] https://lunainc.com/blog/embedded-sensors-can-detect-damage-composites

adjacent to the impact site and directly opposite the impact site on the other side of the vessel. Figure 29 and Figure 30 show the location of the two Bragg gratings and the impact site.

Strain measured by each of the HD-DFOSs after the initial and final impacts are shown in Figure 31 and Figure 32, respectively. Although small, the strain at the impact site is clearly observed below the surface of the overwrap. Note that the damage locations do not line up because the sensors are not precisely aligned, not necessarily because the damage is distributed at different locations within each wrap. Although Fig. 31 shows the impact location relative to the HD-DFOS layout relative to the surface sensor, note that no data is reported for the surface sensor. That sensor was broken during the setup of the experiment. The impact site was located near the second hoop-oriented segment because, although the sensors could not be precisely aligned the position of the second hoop segment of each sensor was deemed to be the most consistent between layers.

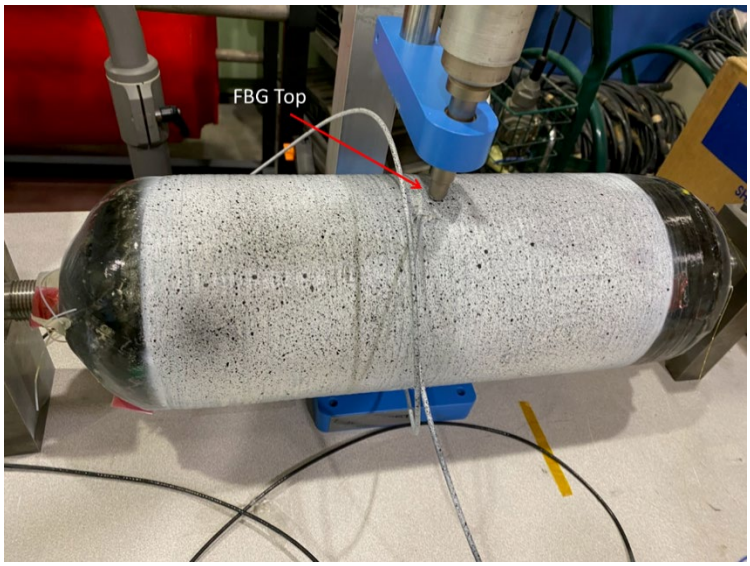

FIGURE 29: PICTURE OF THE IMPACT SITE AND THE FBG BOUND TO THE TOP OF THE VESSEL, ADJACENT TO THE IMPACT SITE. NOTE THAT THE FBG IS ORIENTED TO MEASURE HOOP-DIRECTION STRAIN

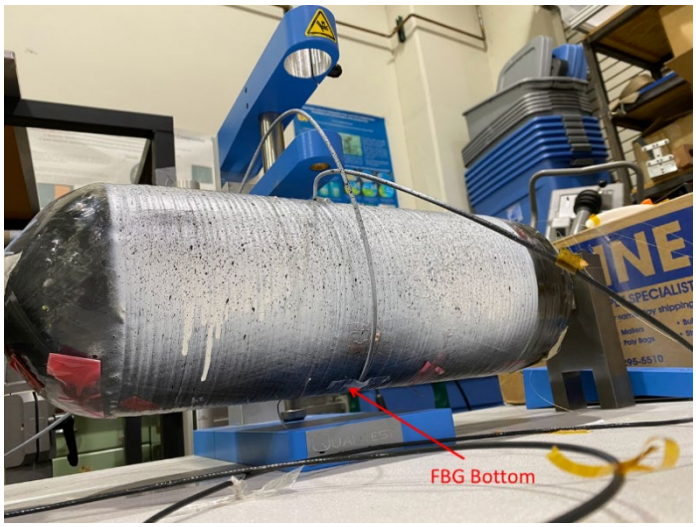

FIGURE 30: PICTURE OF THE IMPACT SITE AND THE FBG BOUND TO THE BOTTOM OF THE VESSEL, ADJACENT TO THE IMPACT SITE. NOTE THAT THE FBG IS ORIENTED TO MEASURE HOOP-DIRECTION STRAIN

Interestingly, two distinct peaks are apparent in the profile from Sensor 3 (Fig. 31). These correspond to locations at the middle of the second hoop-oriented segment and the middle of the first axial segment. These locations are not close to each other, which suggests that delaminations are not limited to the impact site. This is corroborated by the active thermography scans (Fig. 39) which show several delaminations located far from the impact site. The peak in the first axis-oriented segment is not observed in the other two sensors. The sensors are not aligned, so it is possible the axis-oriented segments of the other two sensors are not positioned to detect the distant delaminations.

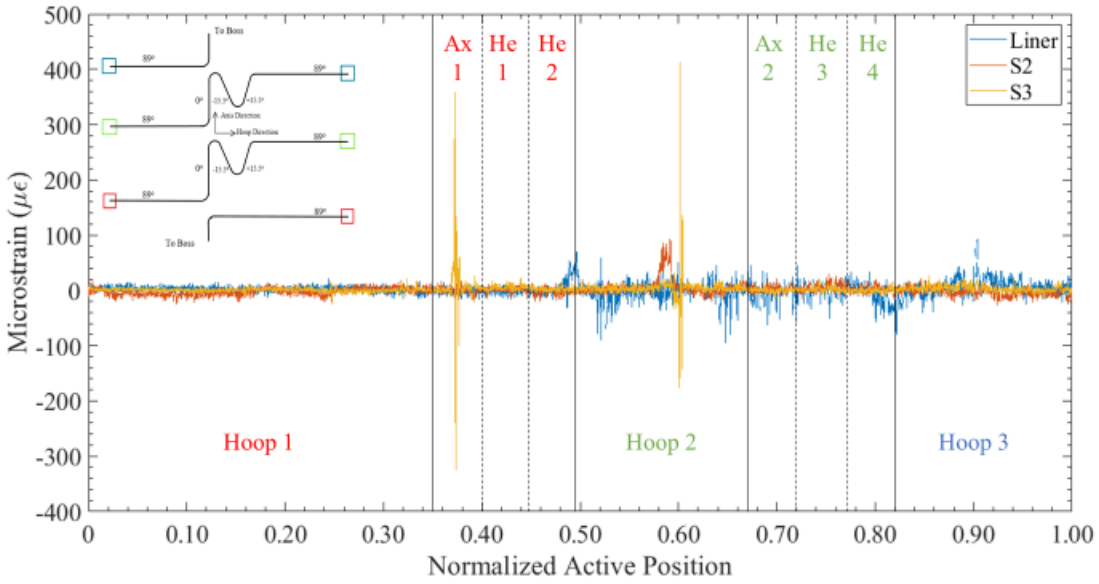

(a)

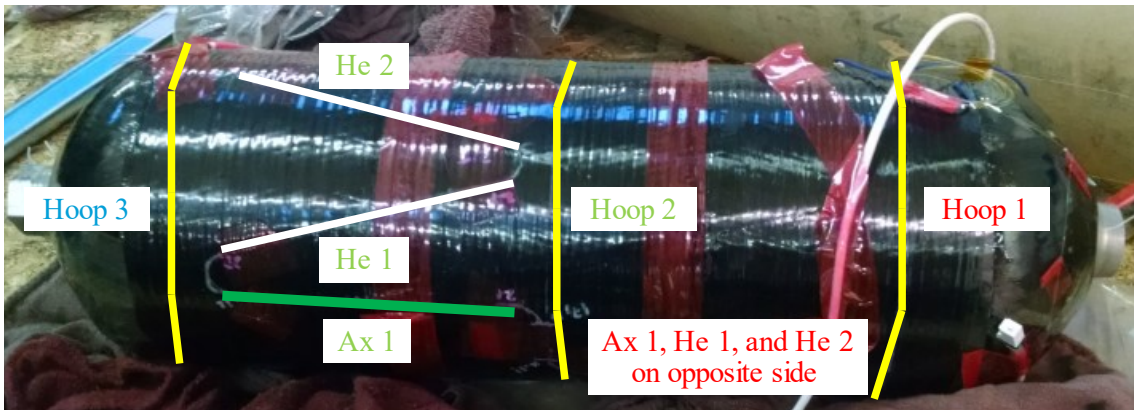

(b)

FIGURE 31: STRAIN PROFILE IN THE STEB WITH EMBEDDED SENSORS AFTER THE 5 J IMPACT AND PHYSICAL LOCATION OF IMPACT SITE ON VESSEL

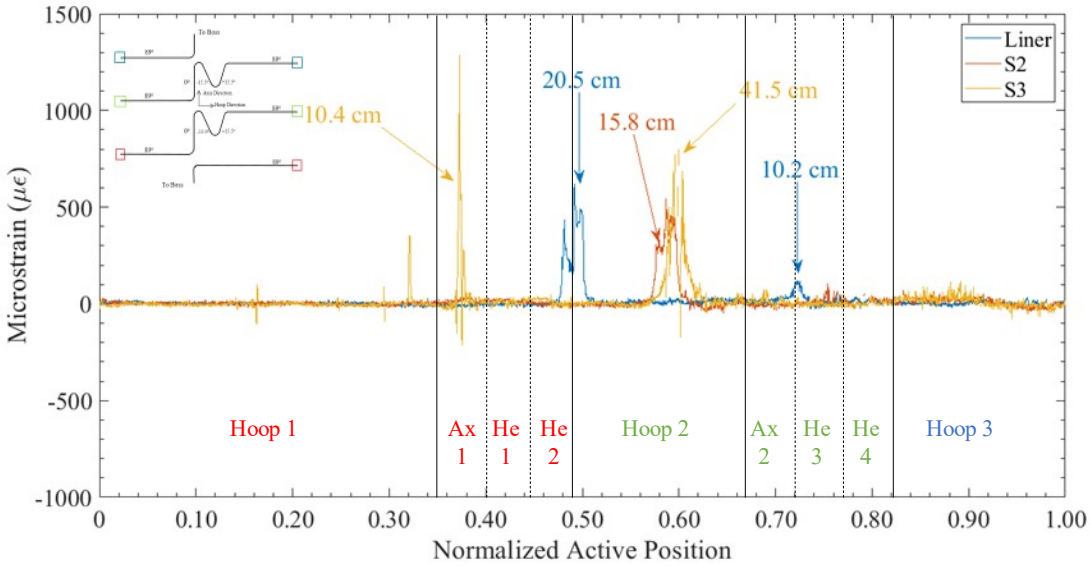

FIGURE 32: STRAIN PROFILE IN THE STEB WITH EMBEDDED SENSORS AFTER ALL IMPACTS. NUMBERS INDICATE THE WIDTH OF THE PEAK

Interestingly, damage accrual appears to occur in discrete stages. Figure 33, Figure 34 and Figure 35 show the strain profiles from each HD-DFOS after each impact. From 5-7 J, the strain profiles do not change significantly, but at 8 J, the peaks become significantly wider, and the strains increase. After 8 J, the profiles remain essentially constant. From this, it seems that the HD-DFOSs are well-suited for tracking impact damage, particularly subsurface delaminations.

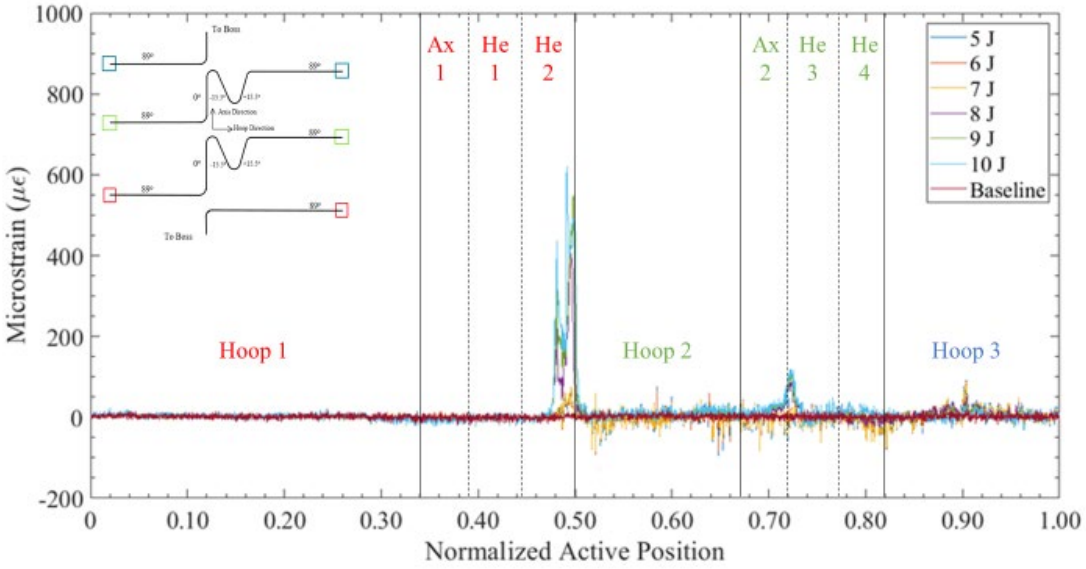

FIGURE 33: SUCCESSIVE STRAIN PROFILES FROM THE LINER-BOUND HD-DFOS

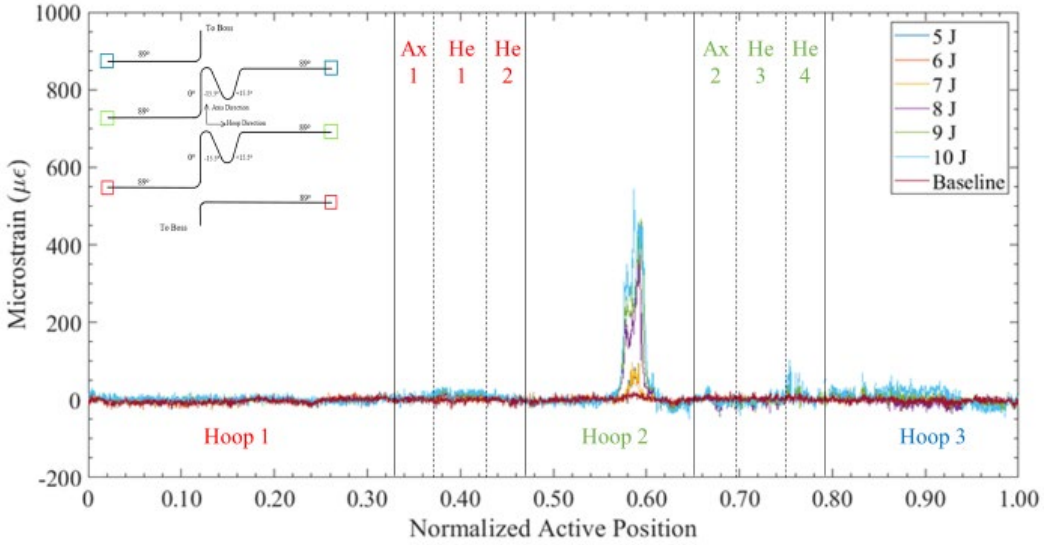

FIGURE 34: SUCCESSIVE STRAIN PROFILES FROM THE HD-DFOS BETWEEN THE FIRST HOOP WRAP AND THE FIRST HELICAL WRAP

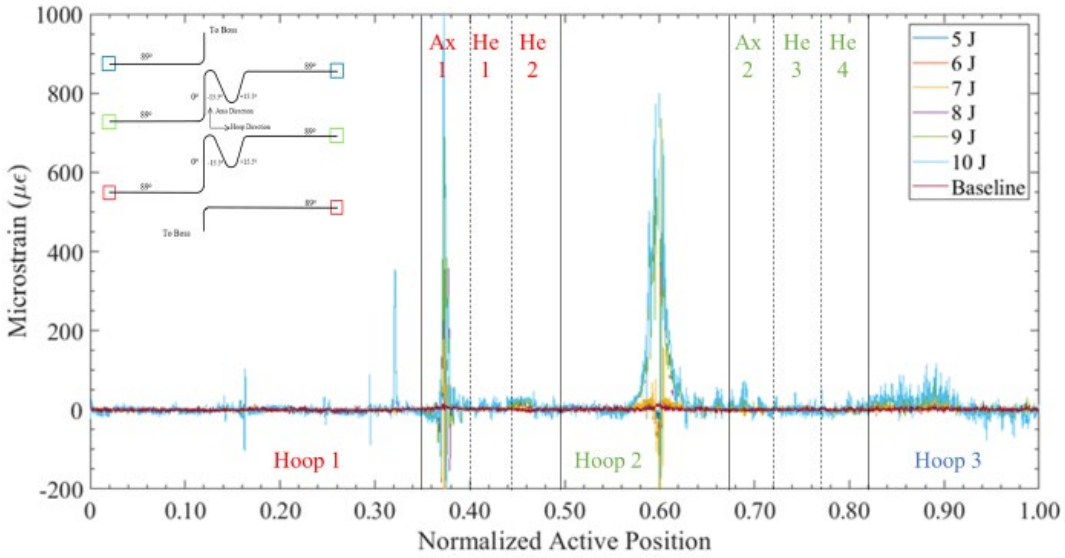

Figure 35: SUCCESSIVE STRAIN PROFILES FROM THE HD-DFOS BETWEEN THE TWO HELICAL WRAPS

One drawback of the spatial resolution offered by the HD-DFOSs is that they cannot acquire data rapidly, simply due to the sheer number of data points collected along the fiber length. The strain measurements will drop out entirely during the impact, so detailed information of how strain travels through the overwrap during an impact is not available. The FBGs are able to measure up to 1 kHz, and so are very useful for acquiring data during impact. Strain measurements from the two FBGs (Figure 36) during the 10 J impact reveal that both the initial impact and the subsequent rebound send waves through the composite overwrap. The wave near the impact site is significantly more damped than the wave at the bottom of the vessel, and there is a slight delay between the two waves. Further investigation is needed to determine if this delay captures the travel of the impact wave. Regardless, this data will be useful for informing FEA modeling of impacts.

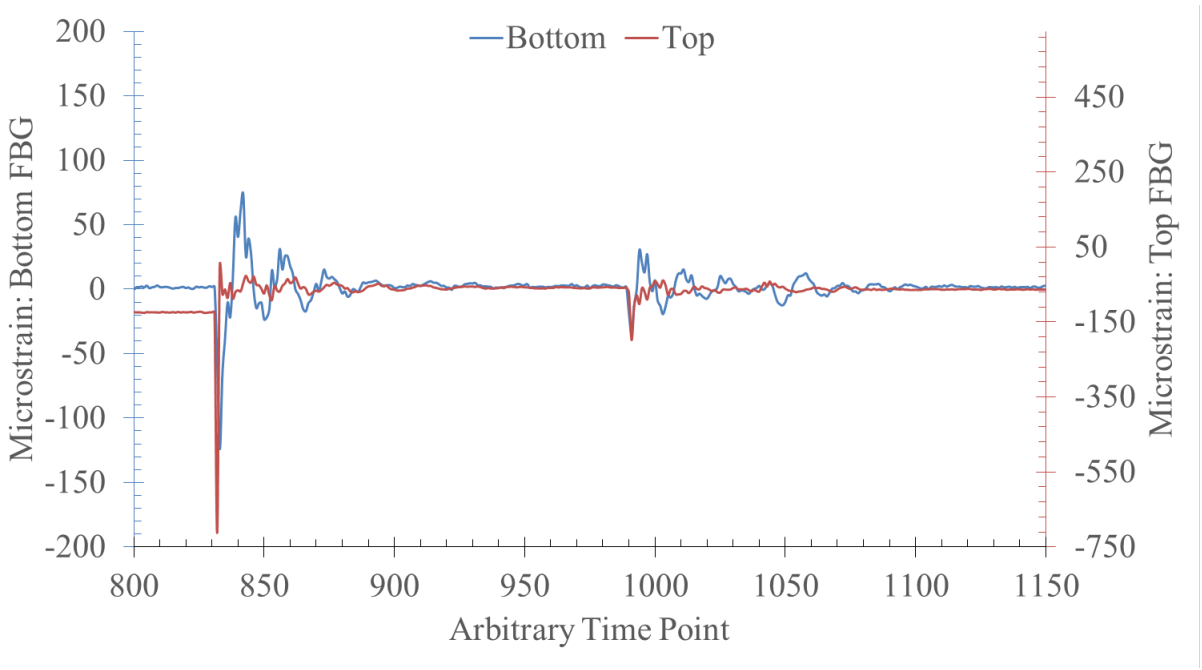

FIGURE 36: STRAIN MEASUREMENTS FROM FBGS LOCATED ADJACENT TO IMPACT SITE (TOP) AND DIRECTLY OPPOSITE THE IMPACT SITE (BOTTOM). SAMPLING RATE WAS 1 KHZ. BOTH SENSORS ARE BOUND TO THE SURFACE OF THE VESSEL

Strain measurements from DIC after impact seem to corroborate the measurements from the HD-DFOSs and FBGs in that it appears the most severe damage to the overwrap is isolated to the immediate vicinity of the impact site. Strain distribution on the surface of the STEB is shown in Figure 37 and Figure 38. When the vessel was at rest, strain measurements were within a $\pm$100 με window around zero. Strain measured at discrete points around the 5 J impact site fell within this window, suggesting that damage was limited to the impact site. This agrees with the measurements from the HD-DFOSs, which show no change in strain measurements outside of the impact site. After the 10 J impact, significant strains were recorded at discrete points at a distance from the impact site, suggesting that the damage had spread over the course of the repeated impacts, which is also suggested by the HD-DFOSs. Virtually all of the strain measurements across the STEB surface fall below 1% strain, making it likely that only very careful visual inspection would be able to ascertain the extent of damage from the low energy impacts. On the other hand, the damage to the vessel is readily observed from the HD-DFOS strain profiles.

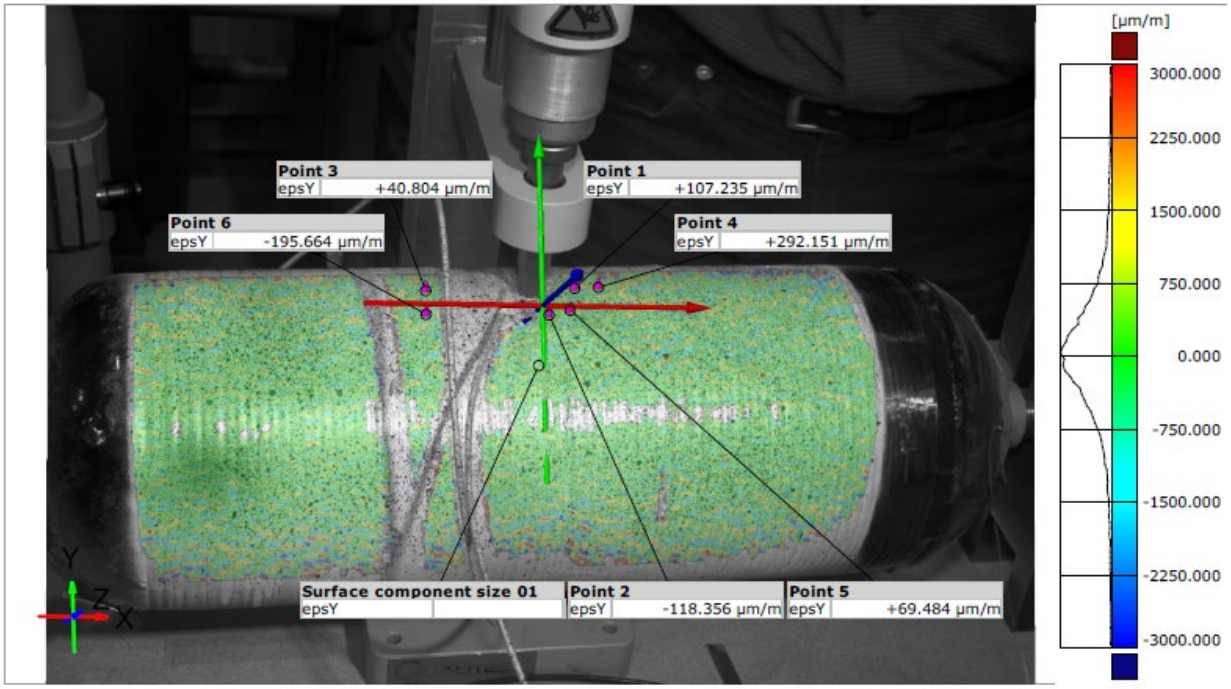

FIGURE 37: HOOP-DIRECTION STRAIN DISTRIBUTION ON THE SURFACE OF THE STEB AS MEASURED BY DIC AFTER THE 5J IMPACT. STRAIN MEASUREMENTS AT DISCRETE POINTS ARE ALSO SHOWN

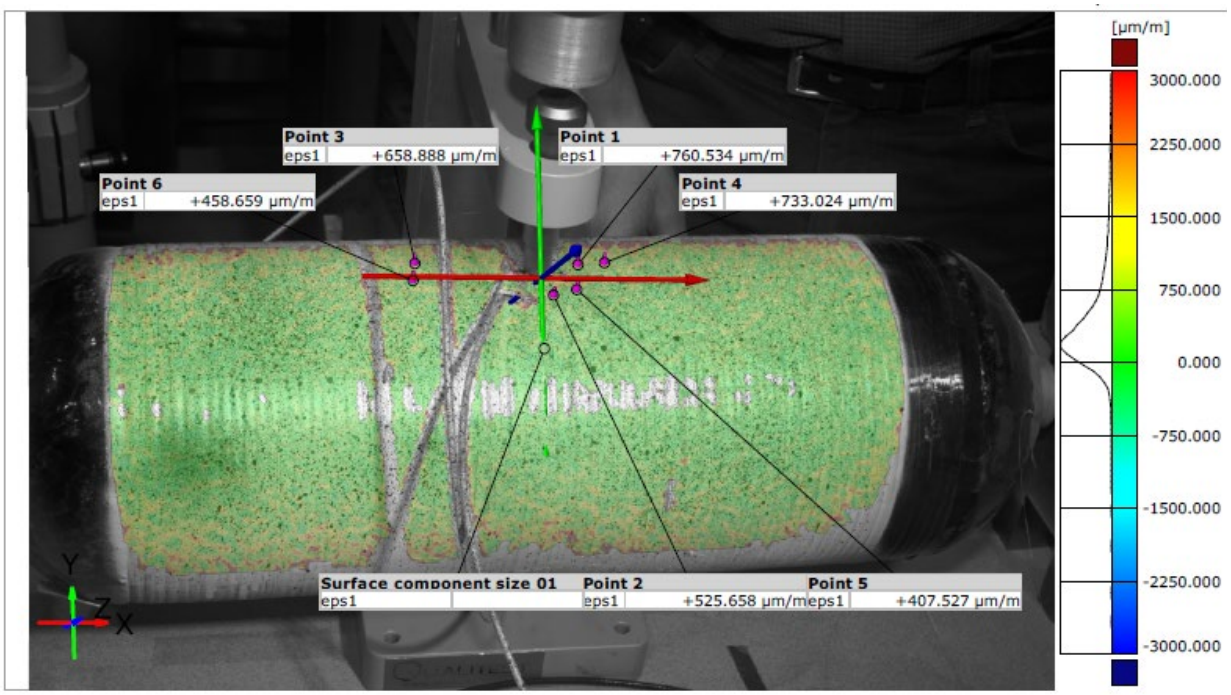

FIGURE 38: HOOP-DIRECTION STRAIN DISTRIBUTION ON THE SURFACE OF THE STEB AS MEASURED BY DIC AFTER THE 10 J IMPACT. STRAIN MEASUREMENTS AT DISCRETE POINTS ARE ALSO SHOWN

While the DFOSs suggest delaminations, the changes in the strain profile after impact do not necessarily correlate with delamination. To determine if there is a direct correlation, the same STEB was subjected to active thermography. This is a technique where a surface is flashed with high energy light, and IR cameras measure the subsequent change in surface temperature as thermal energy diffuses into the overwrap. Regions where through-thickness dissipation is slow correspond to delamination due to the dramatic change in thermal diffusivity between the composite material and the empty air in the delamination. All active thermography was performed by Thermal Wave Imaging at their Detroit, MI facility.

In Figure 39, the STEB was flashed and the first derivative of the IR amplitude was measured over time, with selected time steps shown to demonstrate how thermal energy diffused through the overwrap. At 0.333 s, two lobes are observed at the impact site. These lobes correspond to regions of high stress predicted by FEA and the lobes do not persist through the measurement, suggesting that they are isolated to the surface of the wrap. At 3.899 s and until the end of the recording, a large white spot is observed at the impact site, suggesting that the impact caused delaminations deeper within the overwrap and covering an area much wider than the impact site alone. This pattern is typical of impact damage.

One interesting feature is the V-shaped distribution of delaminations to the right of the impact site that are visible from 1.533 s to 5.332 s. That they do not persist throughout the recording suggests that they are located towards the middle of the overwrap, and the V shape appears to follow the winding path of the helical layer. Together, these observations suggest that the delaminations could correspond to weak spots at the interfaces of the helical layers. This is a critical observation, as it shows that damage from impact, even impacts below 10 J, can induce delamination well beyond the impact site.

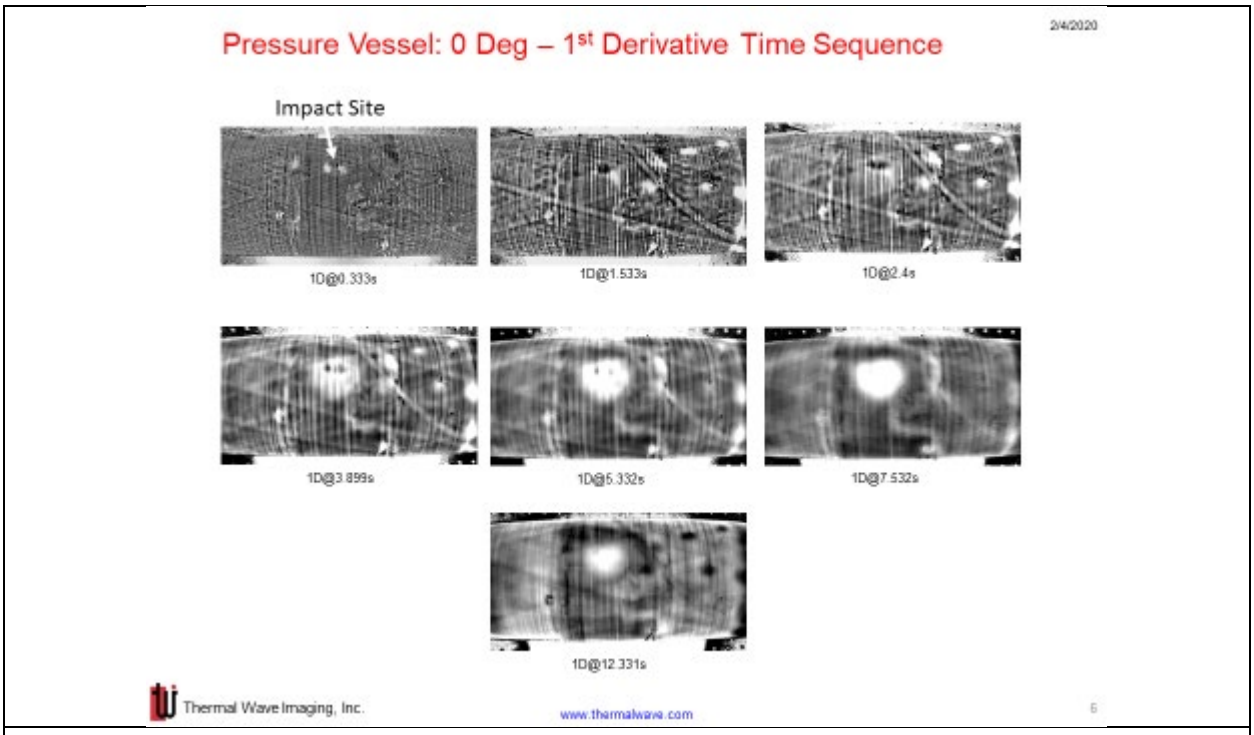

FIGURE 39: TIME-LAPSE SEQUENCE OF THE FIRST DERIVATIVE OF THE IR AMPLITUDE AT SELECT TIME POINTS. WHITE REGIONS DENOTE SLOW TEMPERATURE DISSIPATION. NOTE THAT THE TIME POINTS EFFECTIVELY PROVIDE A THROUGH-THICKNESS VIEW OF SUB-SURFACE DAMAGE

The region with the V-shaped distribution of delaminations corresponds to the region in the DFOS profiles before the main peaks observed at a Normalized Active Position of 0.5 (liner) or 0.6 (S2 and S3). Notably, neither the liner-bound DFOS nor S2 have significant features in their respective profiles in the region with the V-shape-distributed delaminations, whereas S3, located at the interface between the helical wraps, features several peaks in this region, particularly around a Normalized Active Position of 0.38. Without being able to directly trace out S3's position in relation to the delaminations, it is difficult to directly correlate the profile peaks with delaminations and to determine how much the delaminations influence the strain in the surrounding volume. However, given that the strain changes from the delaminations in this region are limited to S3 (nothing was observed in this region in the other two DFOSs), it would appear that the delaminations are limited to this interface and only influence the baseline strain in their immediate vicinity. Future work will need to find a way to keep track of how the DFOSs are laid down in space. This will greatly improve the ability to correlate damage independently observed from NDE to strain features in the DFOS profiles, which will further improve confidence in the ability of DFOSs to measure delamination.

Heavier impacts were also considered. The STEB with a single, surface-mounted sensor was subjected to a 488 J impact using the impact frame in Figure 40 and Figure 41. This test more closely resembles a typical drop test to which COPVs are subjected for post-impact burst pressure. The frame was built at UTK and consists of a 32.6 kg (72 lbs.) impact head assembly (i.e. 11.3 cm (4.5 in) diameter steel cylinder and bar bolted to sliding bearings), a guide frame, and a maximum 1.52 m (5 ft) drop height. To make room for the impact head, the DFOS on the STEB surface was reconfigured to a new layout, shown in Figure 42. Note that the left side Figure 42 is the side of the COPV facing the camera in Figure 40 and Figure 41. The STEB was subjected to a single impact from the maximum 1.52 m (5 ft) drop height, leading to a drop energy of 488 J.

FIGURE 40: HEAVY IMPACT FRAME

FIGURE 41: STEB USED IN THE HEAVY IMPACT TEST

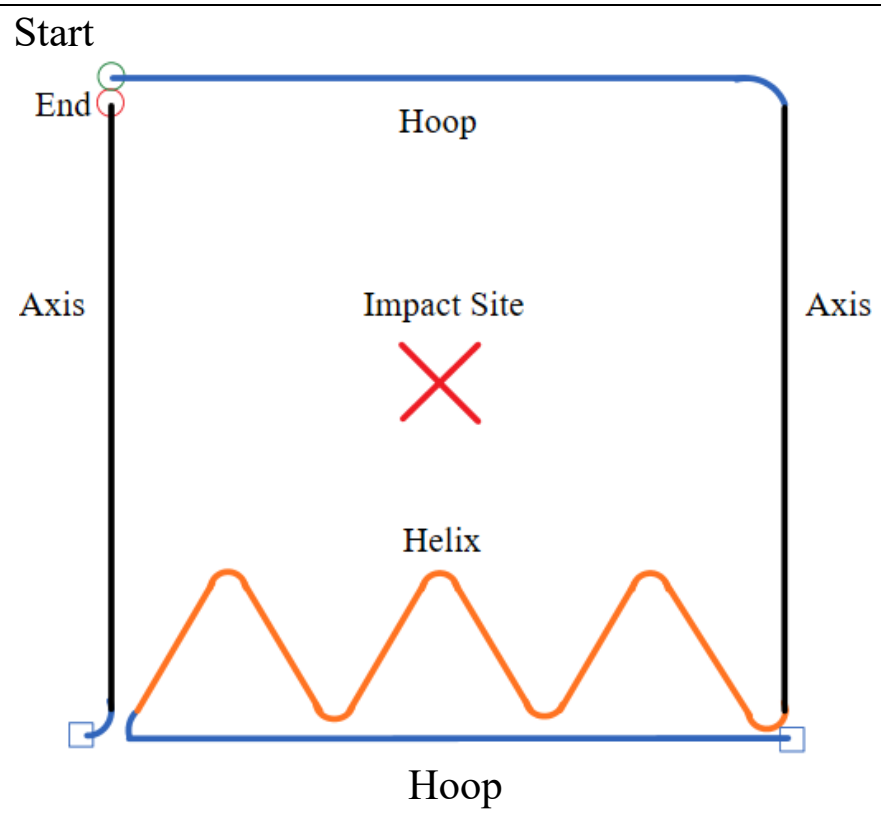

FIGURE 42: LAYDOWN PATH FOR THE FIBER OPTIC SENSOR FOR THE STEB SUBJECTED TO HEAVY IMPACT. THE LEFT SIDE OF THE SCHEMATIC IS THE SIDE FACING THE CAMERA IN FIGURE 40 AND FIGURE 41. DRAWING NOT TO SCALE

The post-impact strain response is shown in Figure 43. A very complex strain profile is observed over the entire overwrap. The two hoop segments have a similar response. Hoop strains are essentially in tension but seem to decrease along the length of the DFOS. The helix segments seem to follow a periodic pattern oscillating around 0 strain. Particularly interesting is that the axial segments recorded very different responses. The first axial segment is essentially under compression, whereas the second axial segment recorded a periodic response similar to the helix segment.

It is not clear from visual inspection what gives rise to this behavior. Indeed, there is almost no visual evidence that an impact occurred, and yet there is a significant change in the strain profile on the surface of the overwrap. This might be the result of a complex distribution of sub-surface delaminations, perhaps a more dramatic version of what was observed in Figure 39. Considering the step-change in strain profile observed with the light impacts, and the complex strain profile from the heavy impact, it seems that impact-driven delamination is not a linear process, rather a product of impact energy ranges, impact history, and perhaps winding pattern. Further investigation with controlled impacts could shed further light onto the initiation and propagation of impact-born delaminations, which DFOSs seem to be well-suited to aid, so long as they are supplemented with NDEs that can identify delaminations.

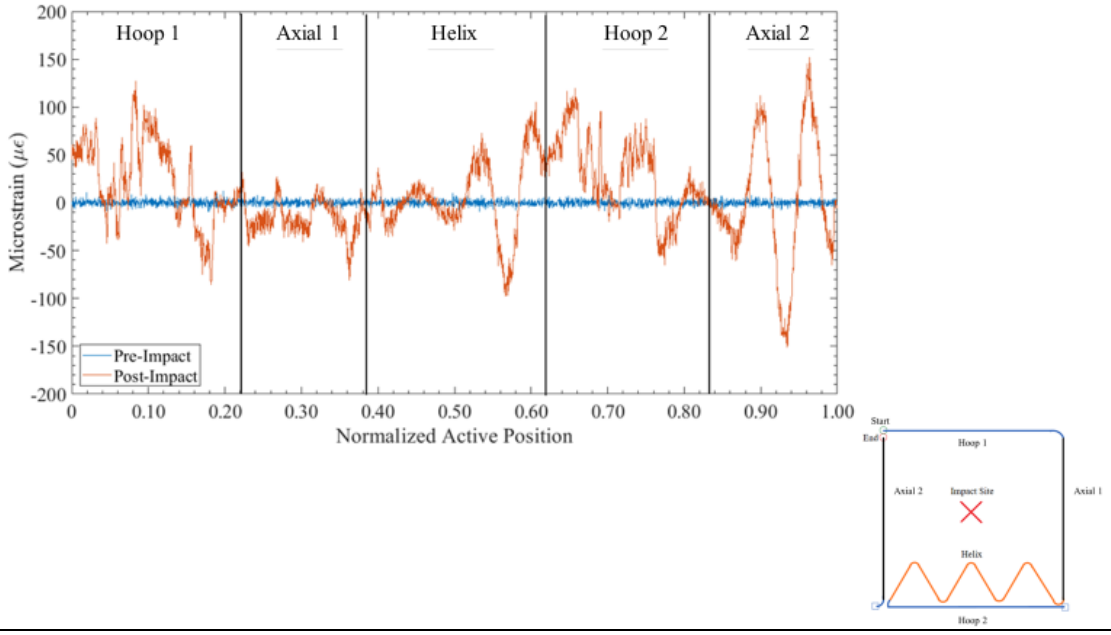

FIGURE 43: STRAIN PROFILE IN THE STEB BEFORE AND AFTER THE HEAVY IMPACT

Because composite-overwrapped pressure vessels are often used in transportation, they can travel over long distances and are subjected to changes in temperature, humidity, and pressure. The ability to track and record the vessel's history is invaluable for predicting the remaining service life of the vessel. To this end, UTK designed and made a wireless sensing module that can measure temperature, humidity, acceleration along two axes, and pressure, and can track how many times the vessel has been filled and emptied. This is all done with a device that has a very small footprint (Figure 44). Data is transferred to a server via cellular towers when a connection is available, and is compatible with 3G and 4G networks, with 5G compatibility planned for future iterations. When a connection is not possible, data is recorded on an internal SD card.

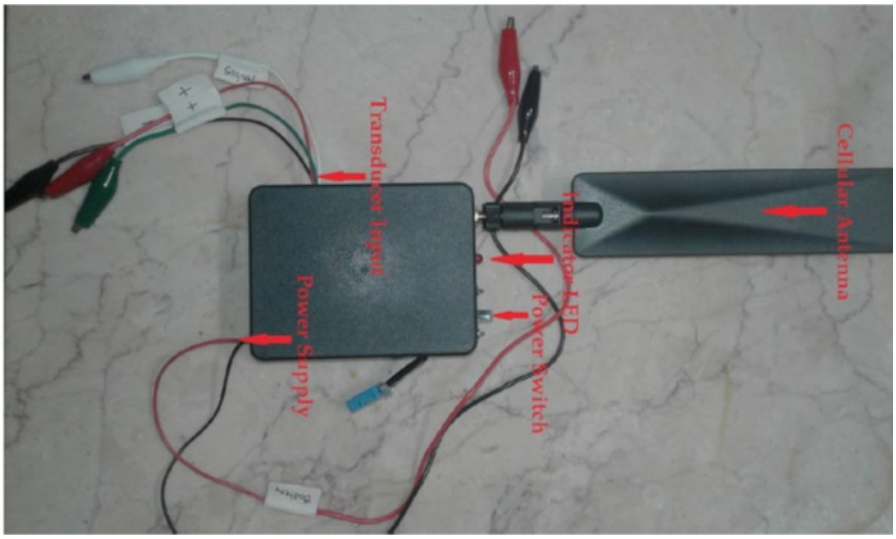

FIGURE 44: REMOTE SENSOR TO MEASURE, TRANSMIT AND RECORD THE INTERNAL PRESSURE, TEMPERATURE, HUMIDITY, AND ACCELERATION OF A COPV DESIGNED BY UTK

The wireless measurement device was tested alongside the full-size vessels. Two measurement sessions were performed: one during the vessel burst test, and one during pressure cycling of the vessel with embedded HD-DFOSs. Results from both are shown in Figure 45 (a) and (b). In both cases, data was successfully recorded and accessed in real time. The pressure readings are not quantitatively correct, but that was a matter of calibration of the pressure transducer. The pressurization trends measured by the wireless unit corresponded with pressure measurements from the circumferential strain gauges on the vessel (Figure 21).

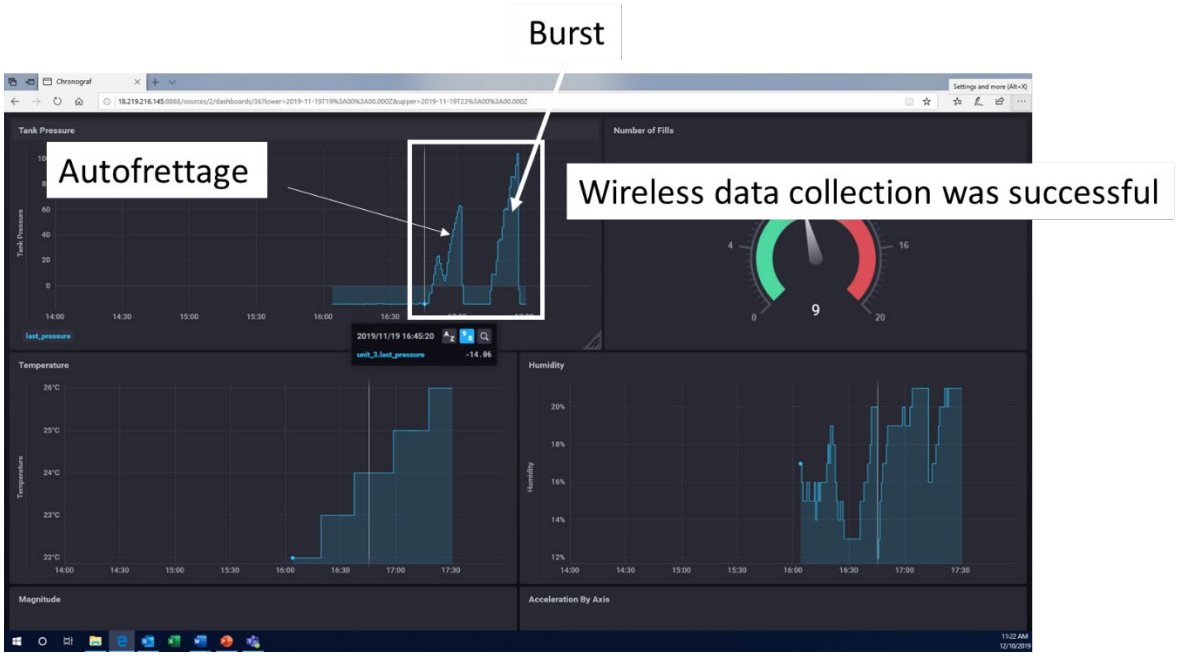

(a)

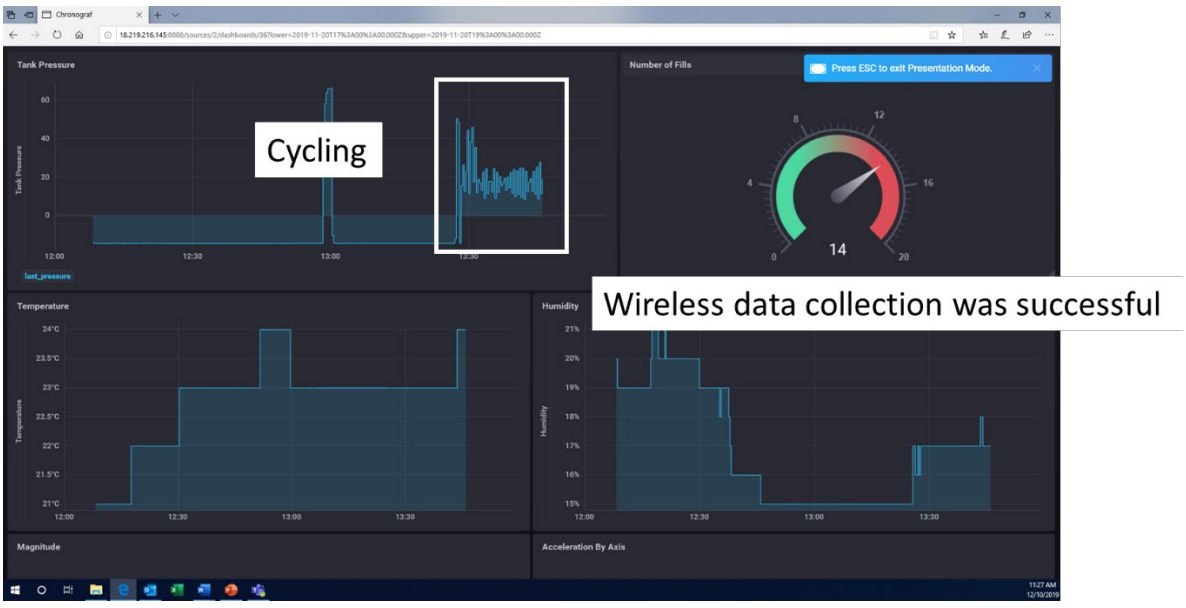

(b)

FIGURE 45: READOUTS OF DATA RECORDED BY THE WIRELESS MEASUREMENT DEVICE. PRESSURIZATION DURING THE AUTOFRETTAGE AND BURST OF ONE VESSEL IS SHOWN ON (A), AND THE PRESSURE OSCILLATIONS FROM THE PRESSURE CYCLING OF THE OTHER VESSEL IS SHOWN IN (B)

5.3 Fabrication and Testing of 80 Liter SCPV with Embedded Sensors

In this task, Steelhead first designed a full size 350 bar (5,075 psi) Type 3 vessel using a finite element (FE) model. Because of the symmetry of the COPV with identical domes and port openings on either end, the analysis is conducted for one half only. The final optimized lay-up sequence of the COPV design was a result of multiple design iterations. The finite element mesh and the material properties of the composite shell are generated using a computer program specifically designed to model filament wound COPVs. It consists of the composite shell and the metallic liner and uses CAX4 axisymmetric elements of the commercial computer program ABAQUS.[6] The model accounts for the following:

- The orthotropic properties of the composite layers in the filament wound cylindrical shell
- The orthotropic properties and thickness of each element in the dome
- The polar build-up in helical plies
- The hoop terminations at the transition region
- Non-linear elasto-plastic material behavior of the 6061-T6 aluminum liner

The FEA of the vessel is conducted using a path-dependent nonlinear solution technique that accurately tracks the plastic deformation of aluminum liner as well as progressive damage in the composite during the subsequent pressurization process. The objective of the design exercise was to ensure that the longitudinal strain in the composite plies of the full size vessel at its target burst pressure does not exceed what was found in the STEB testing for ITS50-24K fiber. Figure 46(a) shows the FEA model and (b) shows the contour plot of the longitudinal fiber strain (%) in the composite at the target burst pressure 865 bar (12,548 psi).

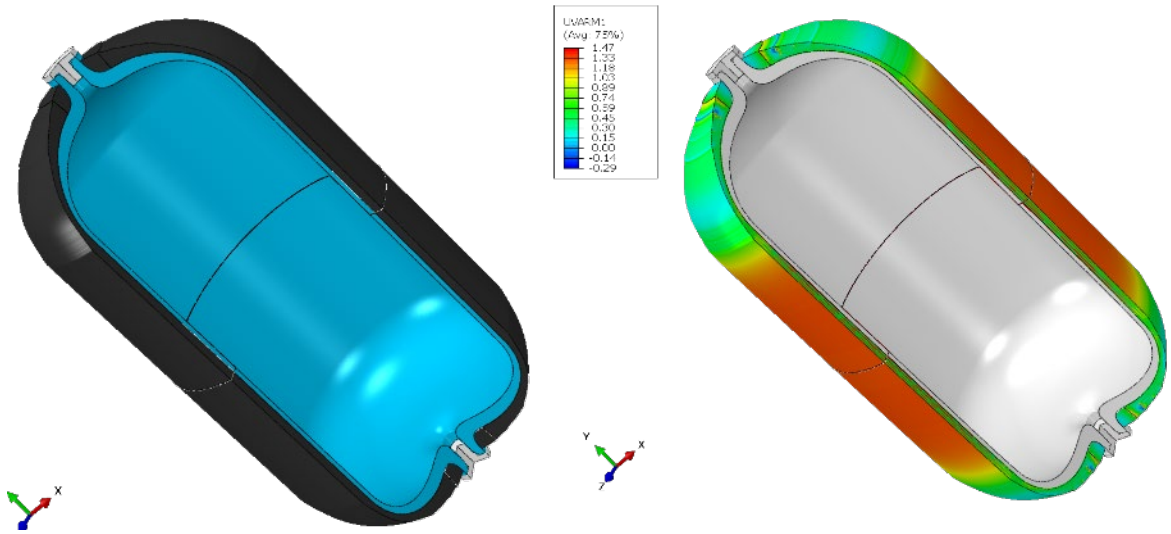

(a) (b)

FIGURE 46 – (A) FINITE ELEMENT MODEL OF THE COPV AND (B) CONTOUR PLOT OF LONGITUDINAL STRAIN IN THE COMPOSITE PLIES AT TARGET BURST PRESSURE

Subsequent to the design, Steelhead fabricated a full size 80L vessel designed for 350 bar H2 storage using the ITS50-24K towpreg. Steelhead used its 4-axis CNC controlled filament winding machine for the fabrication of the vessel. The vessel was cured and equipped with a resistive strain gage oriented to measure hoop strain.

Subsequently the vessel was pressurized hydrostatically until the final rupture. The final burst pressure was 881 barg (12,776 psi) and the failure mode was a clean rupture in the cylindrical section (Figure 48). Strain data collected from the circumferential strain gages during the burst test validated the design prediction (Figure 26). Therefore, the vessel design was set for two subsequent 80L tanks to be fabricated with embedded fiber optic sensors.

FIGURE 47: A 80 L VESSEL PRODUCED FOR VERIFICATION OF BURST PRESSURE

FIGURE 48: A 80L VESSEL (SN 2885) AFTER BURST TEST

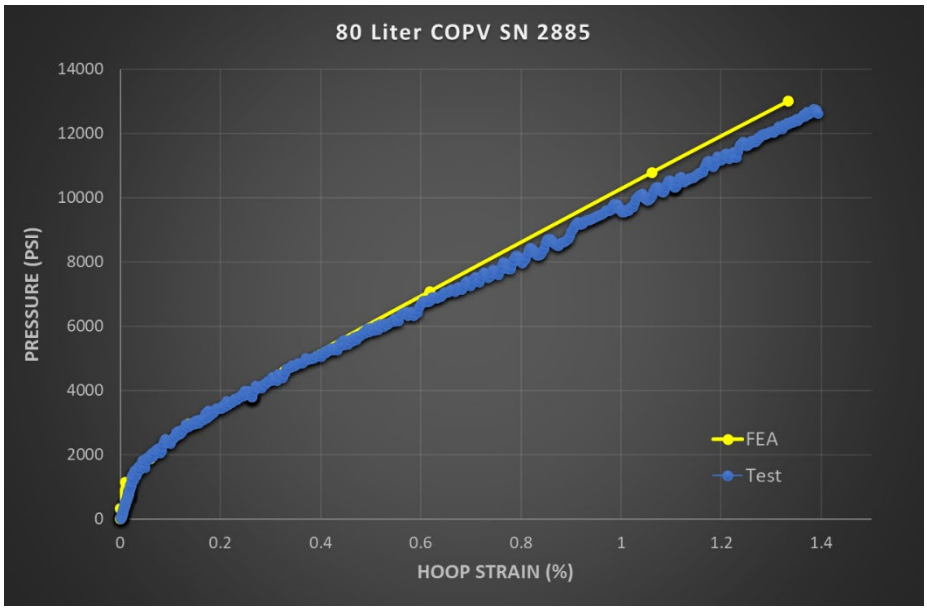

FIGURE 49: CORRELATION OF FEA PREDICTION AND STRAIN GAGE DATA FOR BURST TEST IN 80L VESSEL (SN 2885)

Two full-sized, 80 L vessels were subsequently fabricated (Figure 50) to determine if the observations made in the STEBs scaled up to a larger vessel with a thicker composite overwrap, and to evaluate the SHM potential of the HD-DFOSs in a full-scale pressure vessel. The composite overwrap on the two full-size vessels followed the winding schedule set out in Table 5.

FIGURE 50: TWO 80L VESSELS BEING FABRICATED SIMULTANEOUSLY WITH EMBEDDED FIBER OPTIC SENSORS

One vessel was made with HD-DFOSs embedded at three interfaces within the composite overwrap. Both vessels had a surface-mounted HD-DFOS. All sensors were laid down following the same path used with the STEB with embedded sensors. However, while the helical angle was constant in the STEB, the angle of the helical segments were modified to fit with the local helical angle at the different interfaces of the filament wound layers of the full size vessel.

Unfortunately, the vessel with embedded sensors faced unexpected trouble during the curing step. The viscosity of the resin from the towpreg seemed to have dropped enough to be squeezed out from the composite overwrap and onto the chucks that were used to support the vessel in the winder and the curing oven apparatus (Figure 51). This is the same location where excess HD-DFOS was wrapped to protect it during the winding and curing steps. In order to remove the chucks from the vessel, the HD-DFOSs had to be broken and spliced, which introduces noise into the measurements. The HD-DFOS at the vessel liner was completely lost, and the sensor at the interface of wraps 7 and 8 could not give readings when the vessel was pressurized. The other two HD-DFOSs were recovered, albeit with noisier measurements. Manufacturing strains were the only useful measurements that came out of this vessel. The other vessel with a single, surface-mounted HD-DFOS had no issues and provided the bulk of the data. This vessel was slated for a burst test, and so pressurization was stopped at several intermediate pressures to get strain profiles as a function of pressure.

TABLE 5: WINDING SCHEDULE FOR THE TWO FULL-SIZED, 80 L VESSELS. ANGLES ARE MEASURED FROM THE AXIS OF THE VESSEL.

Layer	*Winding Angle*	*Layer*	*Winding Angle*
Sensor (Vessel 1)		13	90°
1	90°	14	90°
2	90°	*Sensor (Vessel 1)*	
3	90°	15	90°
4	±10°	16	±9°
5	±10°	17	±9°
6	90°	18	±9°
7	90°	19	±21°
Sensor (Vessel 1)		20	90°
8	±10°	*Sensor (Both Vessels)*	
9	±10°		
10	±19°		
11	±25°		
12	±34°		

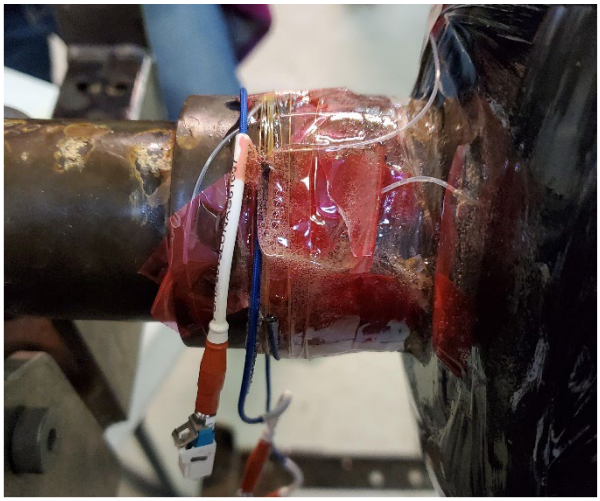

FIGURE 51: RESIN OVERFLOW ONTO THE SUPPORT CHUCKS AND HD-DFOSS

Figure 52 shows the residual strains from winding the full-size vessel with embedded HD-DFOSs (before curing). The profile is similar to the STEB, with the composite overwrap under compressive hoop strain, the liner maintaining its shape, and relatively neutral axial strains. A notable difference from the STEB profile is that the compressive strain at the ends of the vessels is lower than at the middle of the vessel. There was no clear explanation available to explain this phenomenon.

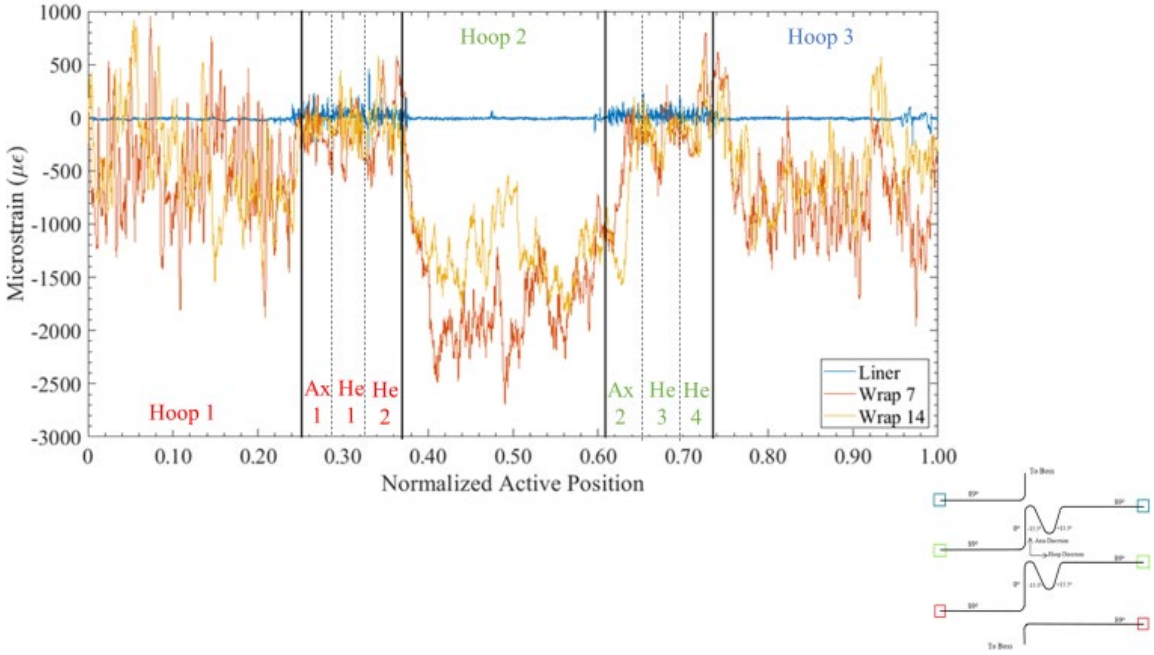

FIGURE 52: STRAIN PROFILES THROUGH THE THICKNESS OF THE COMPOSITE OVERWRAP ON THE FULL-SIZE VESSEL

The influence of the unexpected resin flow is seen in Figure 53 and Figure 54. The residual curing strains in the full-size vessel with a single HD-DFOS (Figure 54) are similar to those observed in the STEB. However, the vessel with embedded HD-DFOSs shows tensile residual strains in the second hoop-oriented segment on both the surface and

at the interface between wraps 7 and 8, but compressive residual strain at the interface between wraps 14 and 15. The team debated on what this indicates. If the middle of the vessel simply squeezed the resin out to its ends by bulging at its center, this would leave all layers in tension, not just two. Regardless, it would appear that if curing runs as expected, the residual strains seen in a STEB are a reliable indicator of the residual curing strains seen in a full-size vessel.

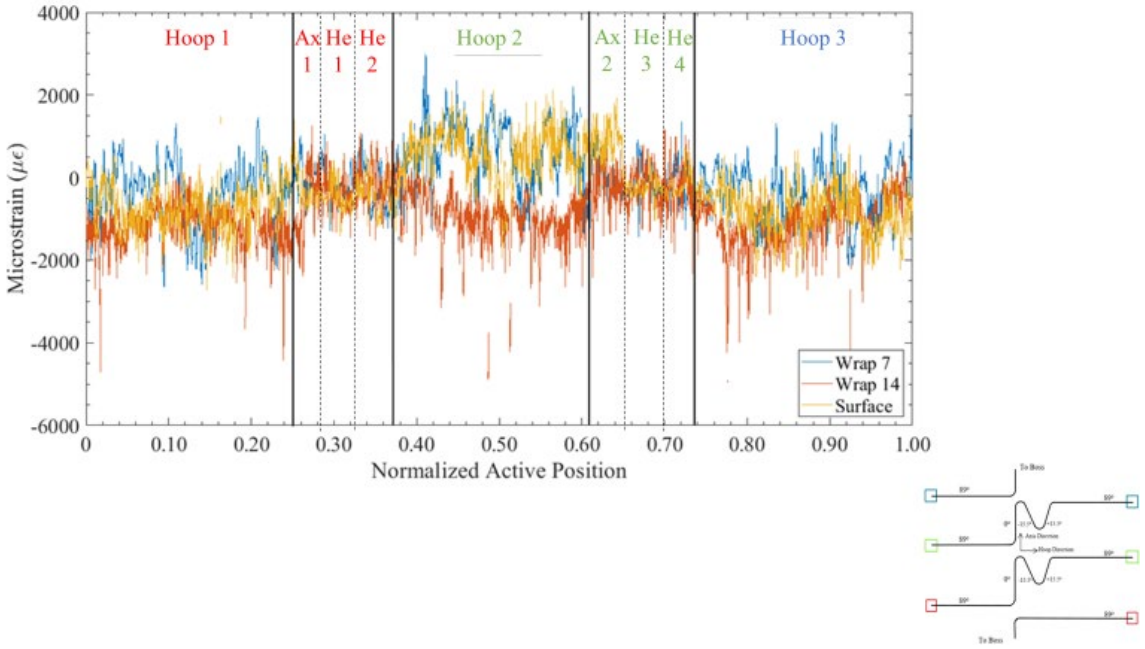

FIGURE 53: RESIDUAL STRAIN AFTER CURING THE FULL-SIZE VESSEL WITH EMBEDDED HD-DFOSS

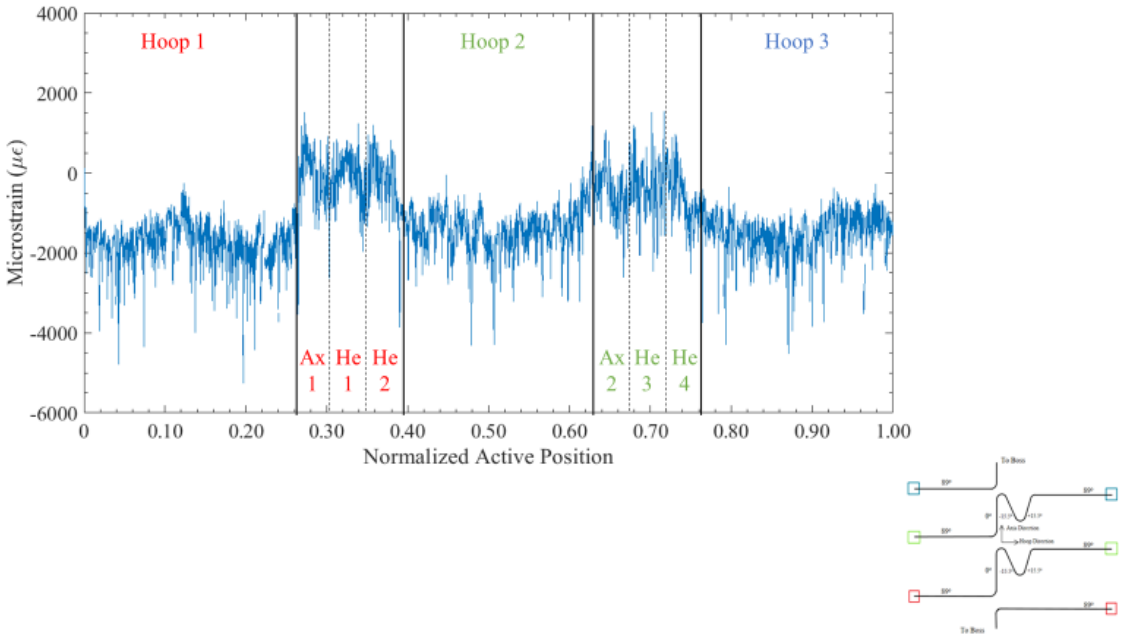

FIGURE 54: RESIDUAL STRAIN AFTER CURING THE FULL-SIZE VESSEL WITH A SINGLE, SURFACE-MOUNTED SENSOR

Figure 55 and Figure 56 show the residual strains after autofrettage of both full-size vessels. Both profiles agree with each other quantitatively, and qualitatively agree with the STEB profile. Again, the composite overwrap experiences tension in the hoop direction. Axial and helical strains are smaller, but also tensile.

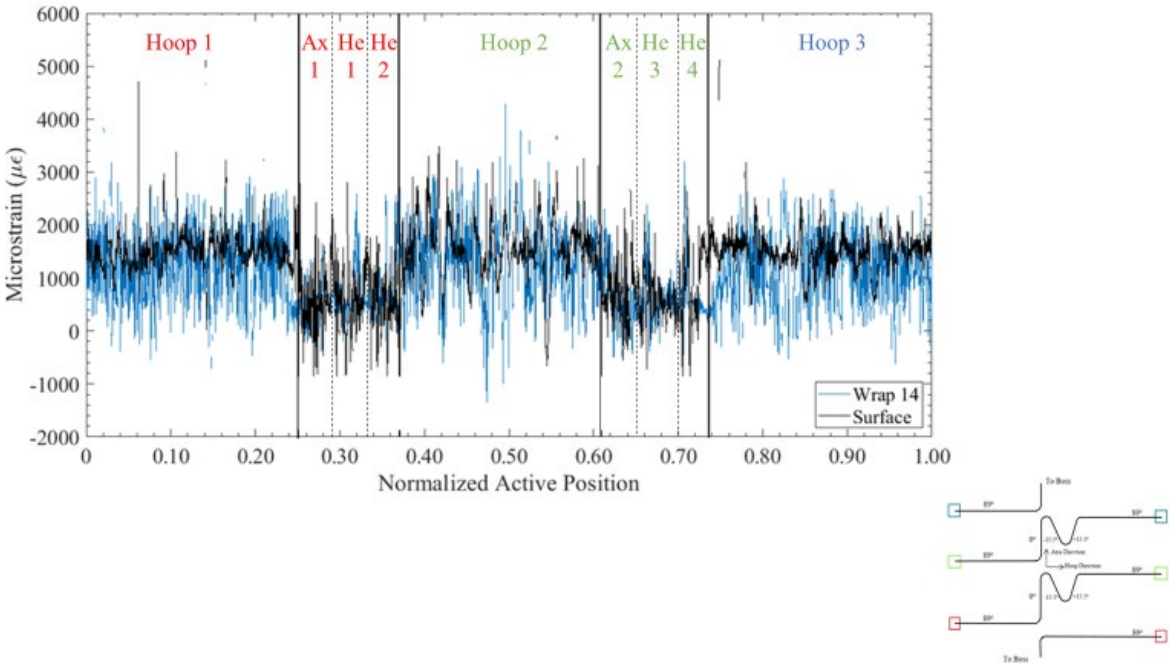

FIGURE 55: RESIDUAL AUTOFRETTAGE STRAINS IN THE FULL-SIZE VESSEL WITH EMBEDDED HD-DFOSS

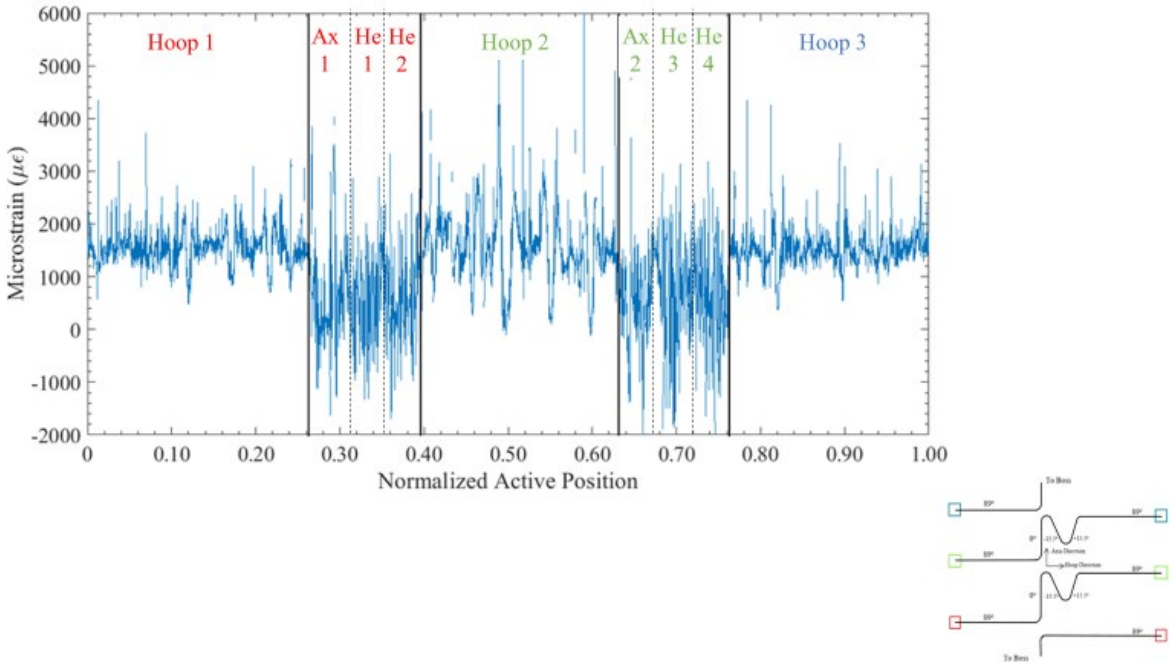

FIGURE 56: RESIDUAL AUTOFRETTAGE STRAINS IN THE FULL-SIZE VESSEL WITH A SINGLE, SURFACE-MOUNTED HD-DFOS

One of the full scale vessels with the HD-DFOS bound to the surface, was filled with water, and taken to the burst testing pit and pressurized hydrostatically to burst (Figure 57).

FIGURE 57: A FULL SIZE COMPOSITE PRESSURE VESSEL IN THE BURST PIT

During the burst experiment, pressurization was stopped at several intermediate pressures to measure the strain on the surface of the composite overwrap with the HD-DFOS, and a RSG mounted near the middle hoop segment of the HD-DFOS (Figure 60). As with the STEB, hoop strain grows faster than the strains along the axial and helical directions. The peaks and troughs in the profile also stay in the same place and increase in magnitude with pressure. Notably, the strains are of the same order of magnitude as the strains measured in the STEB that was burst, yet the pressures are much higher. This makes sense, as the thicker composite overwrap on the full-size vessel should be stiffer than the thinner composite overwrap on the STEB. At 710 barg (10,030 psig) the hoop strains in the middle of the composite overwrap are larger than those near the ends of the vessel, which loosely correlates with the location at which the liner failed.

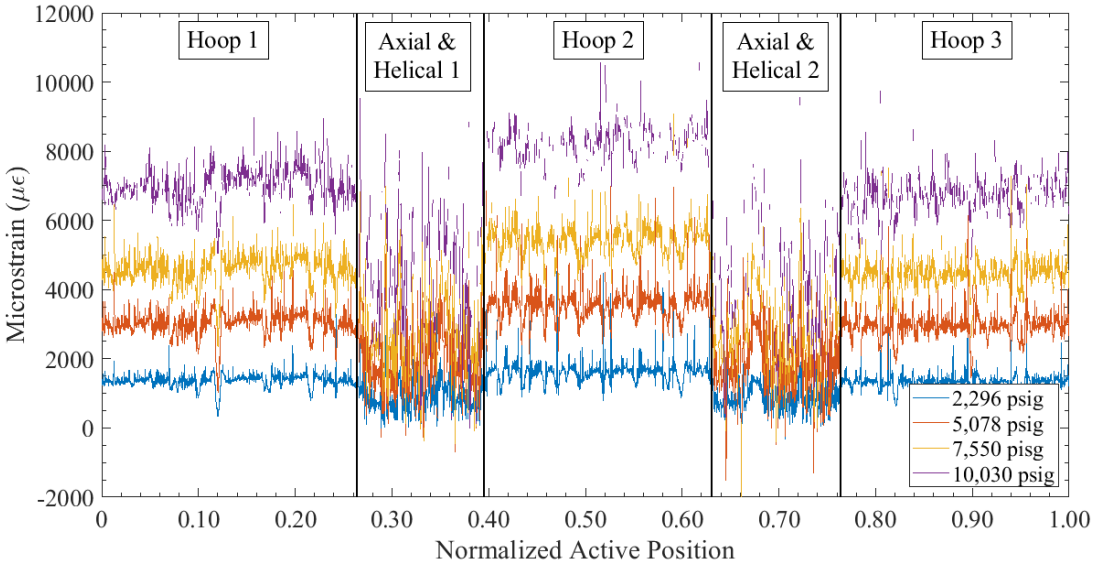

FIGURE 58: STRAIN MEASURED BY HD-DFOS BOUND TO SURFACE OF FULL-SIZE VESSEL IN PRESSURIZATION TO BURST

Although the middle hoop strains are somewhat suggestive of imminent failure, there is no point on the strain profile where strain is growing at a conspicuously faster rate than its surrounding points. In fact, the final measurement before vessel rupture (Figure 59) looks no different than the profile at 10,030 psig. A clear indication of the location of failure was not found in this case. However, failure in composite-overwrapped pressure vessels is borne entirely by the composite overwrap. The failure of the HD-DFOS to identify the location of rupture could be the result of improper placement. An HD-DFOS on or near the liner might sense this damage sooner than a sensor separated from the liner by 20 wraps.

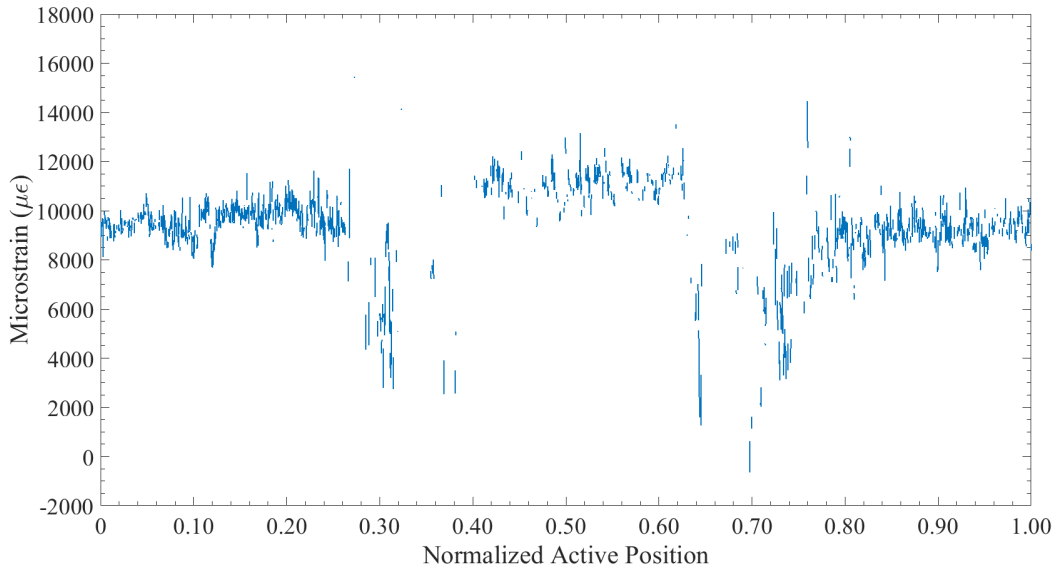

FIGURE 59: FINAL STRAIN MEASUREMENT BEFORE RUPTURE ON THE BURST FULL-SIZE VESSEL

Strain measurements by the HD-DFOS were again supplemented by parallel measurements with a RSG. Although both methods capture the same qualitative behavior, the averaged HD-DFOS strains are consistently lower than those measured by the RSG (Figure 60), as they were with the STEB. In particular, the difference in strain values at burst is significant, roughly 15%.

Although the measured strain profiles did not clearly indicate the rupture location at burst, they can still be useful in identifying points that are less stiff in the composite overwrap. This is illustrated by normalizing and shifting the strain profiles (Figure 61 and Figure 62). Measured strain profiles at the held pressures were normalized to the profile at 158 barg (2,296 psig) and vertically shifted an arbitrary distance to superimpose the profiles. If strain increased evenly with pressure, all of the normalized profiles should be flat lines. However, there are localized peaks in the normalized profiles were strain grows at a faster rate. This could be due to a variety of issues, from the waviness of the towpreg interfaces, to an uneven distribution of resin within the composite overwrap. Even though the resolution afforded by the HD-DFOS might not provide early rupture warning, it can provide insight into how manufacturing affects the composite overwrap's performance.

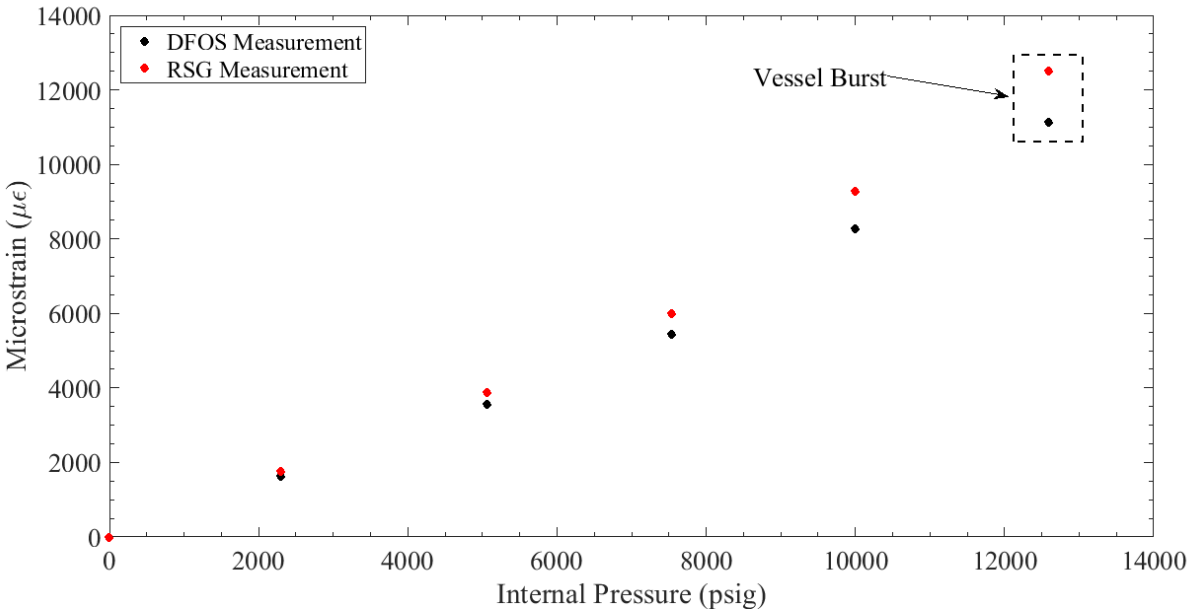

FIGURE 60: COMPARISON OF THE AVERAGED MEASURED STRAIN FROM THE MIDDLE HOOP OF THE HD-DFOS AND THE MEASURED STRAIN FROM A RSG MOUNTED NEAR THE MIDDLE HOOP OF THE HD-DFOS

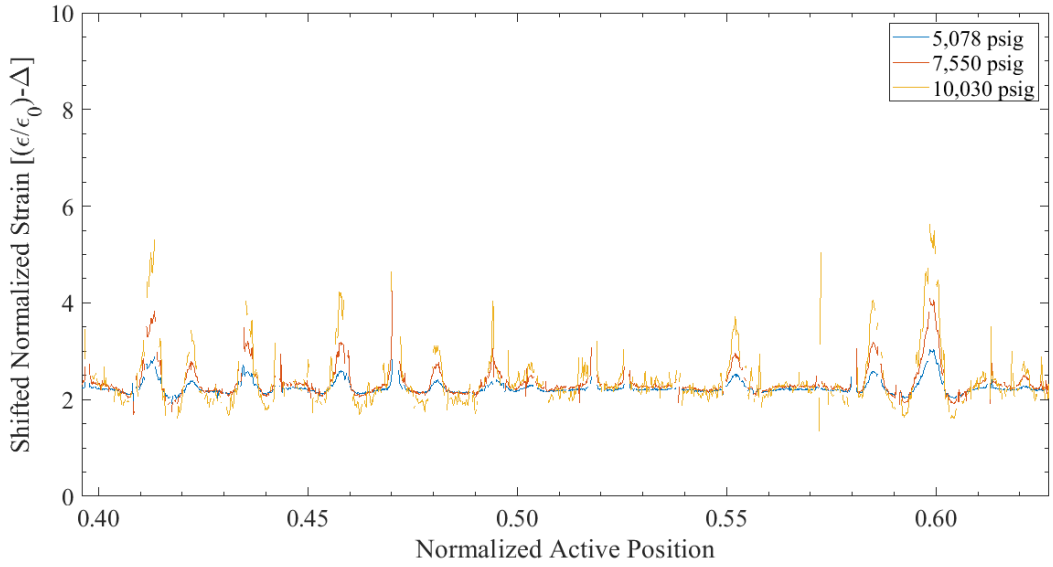

FIGURE 61: PLOT COMPARING THE DIFFERENT STRAIN PROFILES ALONG THE MIDDLE HOOP SECTION OF THE FULL-SIZE BURST VESSEL. STRAIN PROFILES ARE NORMALIZED TO THE STRAIN AT 158 BARG (2,296 PSIG) AND SHIFTED ARBITRARILY TO SUPERIMPOSE THE PROFILES.

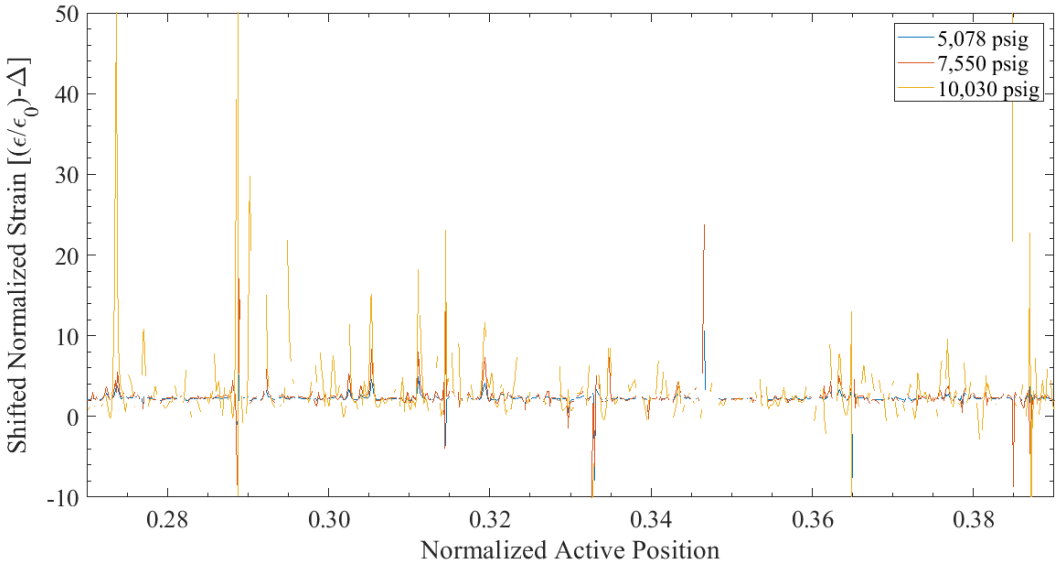

FIGURE 62: COMPARING THE DIFFERENT STRAIN PROFILES ALONG THE FIRST AXIAL & HELICAL SECTION OF THE FULL-SIZE BURST VESSEL. STRAIN PROFILES ARE NORMALIZED TO THE STRAIN AT 158 BARG (2,296 PSIG) AND SHIFTED ARBITRARILY TO SUPERIMPOSE THE PROFILES

6. BENEFITS ASSESSMENT

- One benefit of using the fiber optic sensor is that it can provide extremely granular information about the strain state of the composite shell at multiple locations through the thickness of the composite shell, while the strain gage can only be applied to the surface of the composite.
- Another benefit of the fiber optic sensors is that their granularity seems to be capable of detecting localized delaminations. This is particularly useful for a non-destructive record of vessels over their lifetime as they accumulate delaminations from impacts, and as those delaminations grow because of repeated impacts and, pressure cycling.
- A further benefit of the fiber optic sensor is that its size allows it to be readily embedded into a composite structure, unlike any other NDE sensors. Although this adds more time and manual handling to the winding process, the subsequent evaluations require little more effort than plugging the sensors into the interrogator and result in a highly detailed measurement of the strain throughout the entire 3D structure of the overwrap.
- The benefit of using a remote sensing device that can record and transmit the pressure, temperature, and acceleration of the pressure vessel in real time is recording continuous health monitoring data and status update of the vessel's operating parameters. A device like this will be particularly important when the vessel is involved in a crash or an impact event, when real time data will be needed to make a decision to continue using the vessel or abandon it for safety considerations of the end user.

7. COMMERCIALIZATION

7.1 Market Opportunity

Major auto/truck OEMs are searching for technologies to replace conventional internal combustion engine solutions, there are competing technologies with promise (Figure 63). There are two zero-tailpipe technologies, electric only and hydrogen fuel cells. Electric only vehicles will have a place at all OEM offerings, but due to limited range and lengthy recharging will not be a panacea. Hydrogen fuel cell vehicles, however, offer promise, particularly for larger vehicles and will likely be a major player. A fuel cell vehicle has the convenience of long ranges, quick refueling times and a convenience on par with conventional gasoline/diesel vehicles but with zero emissions. Fuel cell vehicles require a way to store high pressure hydrogen to supply to the fuel cell stack – such as Steelhead's COPVs.

Hydrogen storage is also a key enabling technology for the advancement of hydrogen and fuel cell technologies in applications including stationary power, portable power, and transportation. Hydrogen has the highest energy per mass of any fuel; however, its low ambient temperature density results in a low energy per unit volume, therefore requiring the development of advanced storage methods that have potential for higher energy density.

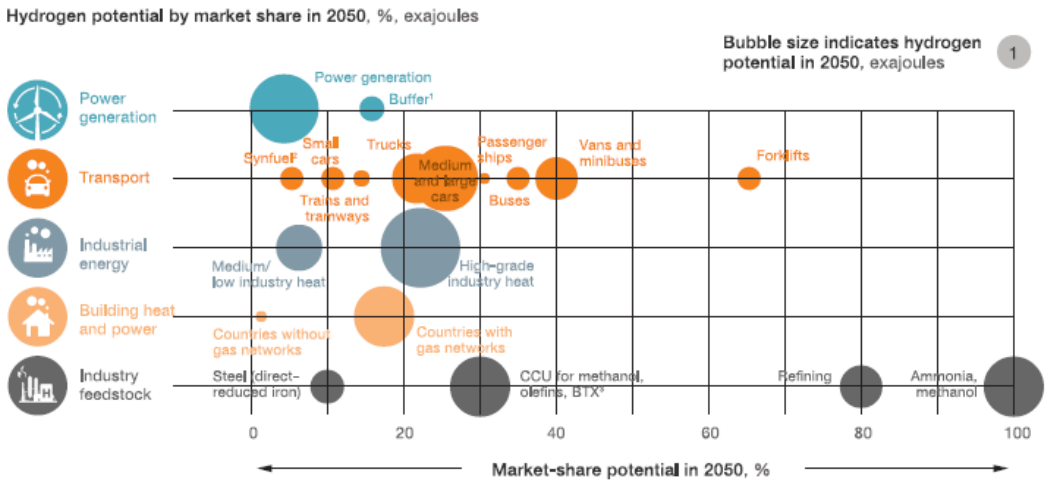

FIGURE 63: PROJECTED H2 MARKET SHARE

Commercialization of hydrogen vehicles has already started for passenger cars, where it is most suitable for larger segments. Three models of FCEVs (Honda Clarity, Hyundai Nexo/ix35/Tucson Fuel Cell, and Toyota Mirai (see Figure 64)) are offered commercially in Japan, South Korea, the United States (specifically, California), and Germany, and ten additional models are slated for release by 2020. Ridesharing or taxi services, which require high uptime, could drive early adoption, and ambitious national targets—such as 1.8 million FCEVs on Chinese and Japanese roads by 2030—could create additional momentum.

Vans and minibuses could also benefit from stringent regulations on delivery vehicles and other commercial fleets in cities. Trucks that carry heavy payloads over long distances are another priority segment. With long ranges and defined routes, they might require less infrastructure: some estimates suggest that 350 filling stations could cover the whole United States. Established manufacturers such as Toyota as well as new start-ups like Nikola Motors have started building heavy-duty and long-haul trucks to capture opportunities in the booming freight-transport industry.

Fuel-cell trains could replace many diesel-powered locomotives on nonelectrified tracks. The first fuel-cell tramway is already operating in China, and the first "hydrail" train by Alstom will start taking passengers in Germany by the beginning of 2018.

FIGURE 64: TOYOTA MIRAI IS A COMMERCIALLY AVAILABLE H2 FUEL CELL CAR

To reach the ambitious 2050 target outlined in the vision, important milestones need to be reached by 2030. The Hydrogen Council estimates that up to one in 12 cars sold in California, Germany, Japan, and South Korea could be powered by hydrogen if major efforts are made to roll out infrastructure and scale up production. Some 50,000 fuel-cell buses and 350,000 fuel-cell trucks could also be on the road globally, saving as much CO2 as some 3.5 million hydrogen-powered passenger cars. The fuel cell market is undergoing significant growth, but still in its infancy. There are currently no clear leaders in component supply and Steelhead Composites sees a significant opportunity to be dominant in the supply chain.

7.2 Commercialization of H2 storage vessels with continuous health monitoring

Steelhead Composites has a significant interest in commercializing composite pressure vessels with embedded telematics and sensors intended for automotive, marine and transportation usage (Figure 65). These sensors will allow for continuous monitoring of the vessel's health, keep an ongoing record of cycle life characteristics, and provide immediate feedback on the vessel's structure in response to any unplanned damage caused by either low or high energy impact. Steelhead Composites is already invested in the vessel design, fabrication, technology integration, certification, marketing, and commercialization. The goal is to commercialize these composite pressure vessels along with the health monitoring technology as an integrated solution to OEMs or system integrators.

The high pressure composite pressure vessel market can be segmented into the following areas – CNG transport vehicles, CNG powered vehicles, hydrogen fuel cell vehicles, and a final category that contains everything from aerospace and industrial applications to self-contained breathing apparatus. In addition to segmenting this market by application, there are significant differences by region, but some trends hold worldwide. For instance, in CNG-capable vessels, the strongest growth will emerge in busses, light trucks, and utility vehicles, while passenger cars are unlikely to become a strong market. This is in contrast to the hydrogen market, where the growth is forecast to be in passenger cars as fuel cells begin to gain better traction especially in California (USA), Japan, China and Korea.

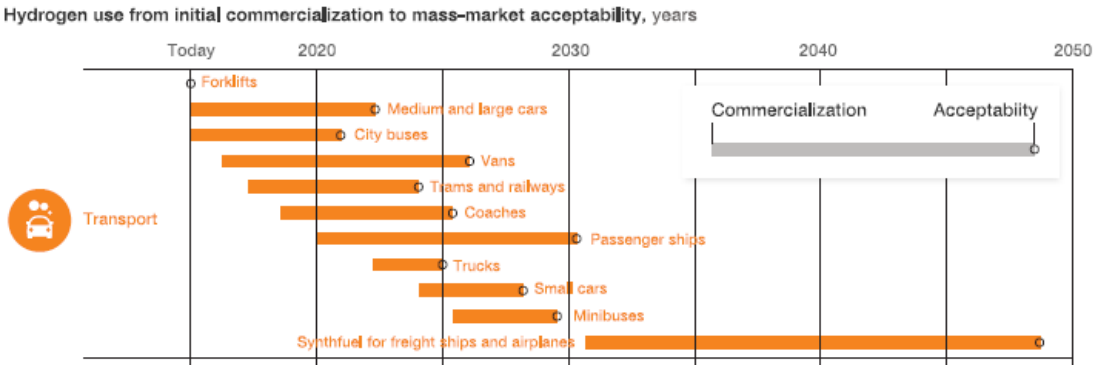

FIGURE 65: PROJECTED GROWTH OF H2 MARKET

The current program has helped to prove the effectiveness of the continuous health monitoring. It is anticipated that the success of implementing integrated health monitoring in composite pressure vessels can attract commercialization opportunities in aerospace and defense applications much earlier than that.

8. ACCOMPLISHMENTS

Over the course of this work, the program team demonstrated the critical steps required to fabricate smart composite pressure vessels with integrated health monitoring.

1. Iterative loops of design and testing using coupons, subscale STEB vessels and full size vessels prove that a new generation of high performance carbon fiber can be used for efficient design of Type 3 vessels for H2 storage.
2. Novel analysis techniques show the promise of predicting the initiation and propagation of interlaminar damage inside the composite shell during the impact damage. Such analysis scheme is typically not used in tank design but is an essential tool for health monitoring of composite vessels.
3. Remote sensing of the key signatures of the tank's operating parameters such as pressure, acceleration and humidity was demonstrated using a unique device that can wirelessly transmit and stream the data to a remote server.
4. Fiber optic sensors were successfully integrated during fabrication of the tanks. These sensors provide a wealth of information regarding the structural health of the vessel when it is subsequently pressurized or subjected to impact damage.
5. Excellent correlation was demonstrated among the fiber optic sensor data, mechanical strain gages and analytical predictions.

9. CONCLUSIONS

The program was able to successfully demonstrate the collaborative power of several engineering disciplines such as material characterization, design and analysis, process development, information systems, testing and data analysis towards a technology that can make composite pressure vessels safe by monitoring its health. However, embedding of these fiber optic sensors during the filament winding of the tanks is a very arduous process and remained an artisan technology at its best at the end of the program. Significant effort needs to be spent in automating or mechanizing the placement of these sensors during the tank fabrication as well as ensuring the

terminations of the sensors are purposefully pre-designed such that it is transparent to the vessel production methodologies.

The program also demonstrated that the granularity of the fiber optic sensors is particularly useful for detecting sub-surface damage within the overwrap of COPVs, especially small delaminations that result from low-energy impacts. This sensitivity has helped show that the initial delamination and its propagation after multiple impacts is a non-linear process, seeming to proceed in distinct steps separated by discrete impact energies. Furthermore, the fiber's sensitivity suggested the delaminations from impact can extend well beyond the impact site, and this was corroborated by active thermography. In fact, even light impacts appear to cause delaminations at apparent weak spots in the overwrap. Heavy impact also resulted in a very complex post-impact strain pattern suggesting a complex distribution of delaminations throughout the overwrap.

10. RECOMMENDATIONS

For further improvements and optimization to be made, work should focus in the following areas:

1. Pre-designed tailoring of the layout of fiber optic sensors (FOS) during the filament winding process can generate spatially sensitive FOS data which can then provide yield meaningful results for interpreting and understanding the health of the tank in service
2. Relating the FOS data to numerical tools through testing and validation that can be used to accurately predict the failure modes of the composite vessels, thereby reduce the "padding" in the factors of safety used by the design standards
3. Delaminations resulting from impact damage can reduce the fatigue life of a composite vessel, which is primarily designed as a tension-loaded structure under internal pressure. FOS sensors can be most effective in interpreting interlaminar delamination in the composite shell of a pressure vessel.
4. Collaboration with fiber optic sensor manufacturers to devise spooling/feeding mechanisms for the sensors that can allow embedding of the sensors in-situ of the filament winding process, without the need to start and stop the process.
5. Validation of the numerical tools developed in this program to predict interlaminar damage of the composite vessel by performing tests with different levels of impact on vessels of different sizes.
6. Assessment of the key advantages and shortcomings of fiber optic sensors and compare them to other incumbent technologies for health monitoring such as acoustic emission, magnetic resonance, shearography etc.
7. Miniaturization of the sensor interrogators that can become integral with the smart tank

11. REFERENCES

1. Fuel Cell Technologies Office Multi-Year Research, Development, and Demonstration Plan – Section 3.2 Hydrogen Delivery.
2. H2@Scale Workshop Report, Proceedings from the H2@Scale Workshop Golden, Colorado, November 16–17, 2016
3. N. Stetson, “An Overview of U.S. DOE’s Activities for Hydrogen Fuel Cell Technologies”, presented at the Materials Challenges in Alternative & Renewable Energy”, Clearwater, FL, February 27, 2012.
4. Adams, J., C. Houchins, and R. Ahluwalia. 2019. “Onboard Type IV Compressed Hydrogen Storage System - Cost and Performance Status 2019,” *DOE Hydrogen and Fuel Cells Program Record 19008*, https://www.hydrogen.energy.gov/pdfs/19008_onboard_storage_cost_performance_status.pdf
5. M. W. Skaar, “Modeling and Testing of Impact Damage in Composite Pressure Vessels”, M.S. Thesis, 2015, Norwegian University of Science and Technology.
6. ABAQUS 2019 User’s Manual.